Metrology for sub-Rayleigh-length target positioning in ~10^{22} W/cm^2 laser-plasma experiments

E.A. Vishnyakov[1], A. Sagisaka[2], K. Ogura[2], T.Zh. Esirkepov[2], B. Gonzalez Izquierdo[2], C. Armstrong[3], T.A. Pikuz[4], S.A. Pikuz[5], W. Yan[6,7], T.M. Jeong[1], S. Singh[8,9], P. Hadjisolomou[1], O. Finke[1], G.M. Grittani[1], M. Nevrkla[1,10], C.M. Lazzarini[1,10], A. Velyhan[1], T. Hayakawa[2,11], Y. Fukuda[2], J.K. Koga[2], M. Ishino[2], Ko. Kondo[2], Y. Miyasaka[2], A. Kon[2], M. Nishikino[2], Y.V. Nosach[12], D. Khikhlukha[1], I.P. Tsygvintsev[13], D. Kumar[1], J. Nejdl[1], D. Margarone[1], P.V. Sasorov[1], S. Weber[1], M. Kando[2], H. Kiriyama[2], Y. Kato[11], G. Korn[1], K. Kondo[2], S.V. Bulanov[1,2], T. Kawachi[2], and A.S. Pirozhkov[2]

[1] *ELI Beamlines Facility, Extreme Light Infrastructure ERIC, Za Radnicí 835, 252 41 Dolní Břežany, Czech Republic*

[2] *Kansai Institute for Photon Science (KPSI), QST, 8-1-7 Umemidai, Kizugawa, 619-0215 Kyoto, Japan*

[3] *Central Laser Facility, Rutherford Appleton Laboratory, STFC, Harwell Oxford, OX11 0QX Didcot, UK*

[4] *Institute for Open and Transdisciplinary Research Initiatives, Osaka University, Suita, 565-0871 Osaka, Japan*

[5] *HB11 Energy Holdings, Freshwater, NSW 2095, Australia*

[6] *Key Laboratory for Laser Plasmas (Ministry of Education), School of Physics and Astronomy, Shanghai Jiao Tong University, Shanghai 200240, China*

[7] *Collaborative Innovation Center of IFSA, Shanghai Jiao Tong University, Shanghai 200240, China*

[8] *Institute of Plasma Physics ASCR, Za Slovankou 1782/3, 182 00 Prague, Czech Republic*

[9] *FZU – Institute of Physics ASCR, Na Slovance 1999/2, 182 21 Prague, Czech Republic*

[10] *Czech Technical University in Prague, FNSPE, Brehova 7, 11519 Prague, Czech Republic*

[11] *Institute of Laser Engineering, Osaka University, 2-6 Yamadaoka, Suita, 565-0871 Osaka, Japan*

[12] *Institute of Physics, National Academy of Sciences of Ukraine, Prosp. Nauky 46, 03680 Kyiv, Ukraine*

[13] *ISTEQ AR, Raffi Street 111, Yerevan, Armenia*

Abstract Tight focusing with very small f-numbers is necessary to achieve the highest *at-focus* irradiances. However, tight focusing imposes strong demands on precise target positioning *in-focus* to achieve the highest *on-target* irradiance. We describe several near-infrared, visible, ultraviolet, soft and hard X-ray diagnostics employed in a ~10^{22} W/cm^2 laser-plasma experiment. We used ~10 J total energy femtosecond laser pulses focused into a ~1.3-μm focal spot on 5–20 μm thick stainless-steel targets. We discuss the applicability of these diagnostics to determine the best *in-focus* target position with ~5 μm accuracy (i. e., around ½ of the short Rayleigh length) and show that several diagnostics (especially, 3ω reflection and on-axis hard X-rays) can ensure this accuracy. We demonstrated target positioning within several μm from the focus, ensuring over 80% of the ideal peak laser intensity *on-target*. Our approach is relatively fast (requires 10-20 laser shots) and does not rely on the coincidence of low-power and high-power focal planes.

Key words: laser-plasma interaction, ultra-high intensity, precise target positioning, spectroscopy, X-rays.

Correspondence to: Extreme Light Infrastructure ERIC, Za Radnicí 835, 252 41 Dolní Břežany, Czech Republic eugene.vishnyakov@eli-beams.eu; Kansai Institute for Photon Science (KPSI), QST, 8-1-7 Umemidai, Kizugawa, 619-0215 Kyoto, Japan pirozhkov.alexander@qst.go.jp.

1. Introduction

Contemporary high-intensity femtosecond laser facilities that are based on the Chirped Pulse Amplification (CPA) concept[1] now reach subterawatt[2], multi-terawatt[3–12] and petawatt[13–20] power levels, with a rapid increase in their number worldwide[21–23]. Most of the high-power

systems are near-infrared (near-IR) facilities taking advantage of Ti:sapphire lasers, while others operate in the mid-IR[2] or visible[9,10] spectral ranges. In certain cases, two-color lasers[11] are advantageous for high-intensity laser-matter interaction experiments.

Tight focusing of intense femtosecond laser pulses into diffraction-limited focal spots or spots with high Strehl ratios $S \geq 0.5$ and small effective radii $r_{eff} \sim 1$ μm enables the transition of the laser-matter interaction to substantially relativistic regimes[24]. One of the important parameters in the interaction processes is the peak laser intensity on-target $I_0 = a_0^2 \times 1.37 \times 10^{18}$ W/cm^2 $\times$ $(\lambda/\mu m)^{-2}$, where λ stands for the laser wavelength, and a_0 is a normalized vector-potential of the laser field – electron interaction. Relativistic regimes correspond to $a_0 > 1$.

Most of the existing high-intensity experiments have been carried out at laser intensities $I_0 \sim 10^{18}$ to 10^{21} W/cm^2 ($a_0 \sim 1$ to 30), and only a few at $I_0 > 10^{21}$ W/cm^2 [25–33]. New regimes of laser-matter interaction require intensities $I_0 \sim 10^{22}$ W/cm^2 and higher, leading to efficient radiation-pressure-dominant ion acceleration at $I_0 > 10^{22}$ W/cm^2 [34,35], radiation damping at $I_0 > 3\times10^{23}$ $(\mu m/\lambda)^{4/3}$ W/cm^2 [24], and quantum electrodynamic effects at $I_0 > 6\times10^{24}$ W/cm^2 [36]. A distant goal is reaching intensities of $I_0 > 10^{26}$ W/cm^2 required for optically-induced vacuum breakdown[37]. Recently an intensity of $I_0 > 10^{23}$ W/cm^2 has been experimentally demonstrated[38]. Advancing laser fields to these numbers requires a comprehensive control of the spatial and temporal envelope of the laser pulses[8,39], as well as placing the target within an extremely short Rayleigh length (~10 μm in our case), which is a consequence of using high-aperture focusing mirrors with small *f*-numbers to attain focal spots with $r_{eff} \sim \lambda$. It is worth mentioning that laser-gas interactions are largely negatively affected by the focal spot

imperfections[40–42], while laser-solid interactions are strongly influenced by laser pre-pulses and pedestals producing pre-plasmas on different timescales[43,44].

Common methods for target positioning include, for example, shadowgraphy, retro-focusing, and direct observation of the rear side of a solid target[45–47]. However, in case of relatively wide and smooth mirror-like reflective tape targets, shadowgraphy cannot ensure target positioning with an accuracy of better than few tens of microns[47]. At the same time, techniques for direct observation of the target surface are most advantageous in the case of single-shot experiments or while operating at low-repetition-rate laser systems that typically deliver up to several full-power shots per hour[47]. In our case of 0.1-Hz laser operation, direct observation of the target surface for the precise target placement would be more time-consuming than using 10-20 full-power laser shots to find the best focus. The techniques we present in our paper can be used in experiments using laser systems with high repetition rates of 0.1–10 Hz, like ALEPH[48] in Colorado, Astra Gemini[49] in the UK, Apollon[50] in France, ATLAS 3000 and PFS[51] in Munich, BELLA[39] in Berkeley, CoReLS[17] in South Korea, Diocles[52] in Nebraska-Lincoln, DRACO[53] in Dresden, HAPLS[54,55] at ELI-Beamlines in the Czech Republic, HERCULES[4] in Michigan, HF-PW at ELI-ALPS[56] in Hungary, HPLS[19,20] at ELI-NP in Romania, SCAPA[57] at the University of Strathclyde in Glasgow, SULF[31] in China, VEGA[58,59] in Spain, as well as commercial PULSAR laser systems in Canada[60], Italy[61] and China[62].

As the laser intensity *at-focus* is tremendously high, direct observation of the focal spot is difficult during the experiment. The focal spot can be measured prior to the experiment by attenuating the high-power laser beam after the amplifiers with the aid of wedges[8] or low-reflectivity mirrors[38] with a controlled surface quality. However, when the focal spot is small

and of high quality, positioning the target within the Rayleigh length becomes non-trivial, since the Rayleigh length is ~10 μm for a typical ~1 μm focal spot and a wavelength of 0.8 μm.

Here we describe our approach to control the tight laser focusing *on-target* using several diagnostics during the target position scan. We show that about 10-20 full-power laser shots were required to determine the best position of the target with an accuracy of ~5 μm, after which we immediately started collecting data at the best *in-focus* target position, with no reliance on the long-term laser stability and absence of the thermal drifts, as well as without any requirements on the focal planes for the low-power and high-power shots to be coincident. The diagnostic instruments employed here covered the IR, visible, extreme ultraviolet (XUV) and X-ray spectral ranges, observing the corresponding radiation from both the front and rear sides of the target. We report on the design of the experimental setup, the methods we used, and the applicability of the diagnostics for target positioning, including the dependence on the target thickness. We demonstrate target positioning within several μm out of the best focus, ensuring over 80% of the ideal peak laser intensity.

2. Experimental setup

The experiment was carried out in the Short-F target chamber of the J-KAREN-P laser facility[7,8] at KPSI, Japan. The p-polarized laser pulses with a central wavelength of $\lambda_0 \sim 820$ nm, duration of 33 fs and energy up to 12 J were focused with an *f*/1.3 Off-Axis Parabolic (OAP) mirror with a 45º deviation angle into a focal spot with an effective radius $r_{\mathrm{eff}} \sim 1.3$ μm. The laser operated at 0.1 Hz, delivering typically several hundred full-power shots per experimental day.

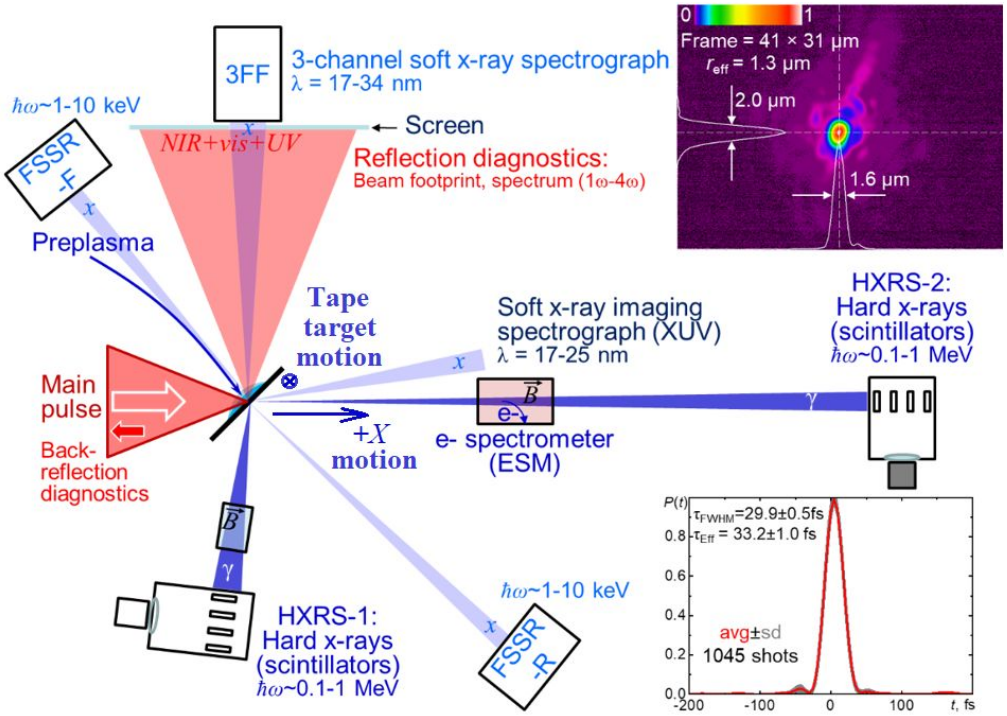

Fig. 1. Experimental scheme (not to scale). The J-KAREN-P laser pulses (Ø 280 mm, 33 fs, 10 J, $\lambda_0 \sim 820$ nm, p-polarized) were focused into an $r_{eff} \sim 1.3$ μm focal spot on a 5 – 20 μm stainless-steel tape target[26] mounted at a 45º incident angle. The observation direction of the back-reflection diagnostics at 1ω is shown by the red arrow. Several reflection diagnostics (1ω and 2ω imagers, 1ω – 4ω fiber spectrometer) measured the reflected beam footprint on a screen mounted perpendicular to the 'specular reflection' direction; a three-channel flat-field XUV spectrograph (3FF) was mounted behind a hole in the screen. The first hard X-ray spectrometer HXRS-1 was mounted 98º off the main laser pulse direction. The second hard X-ray spectrometer HXRS-2 and an electron spectrometer (ESM) were along the direction of the main laser pulse, while the imaging XUV spectrograph was 12º off this direction. $\vec{B}$ symbols stand for dipole magnets removing electrons from HXRS-1,2 and dispersing electrons in the electron spectrometer ESM. Two soft X-ray spectrometers with spatial resolution (FSSR) were mounted out-of-plane on the target front (-F) and rear (-R) sides, respectively. The insets show spatial and temporal J-

KAREN-P laser pulse profiles. A tape target of 20 mm width was mounted on a double-rotating-reel setup, which could be translated linearly along the laser axis with a 0.1-μm step size (the '–' sign denotes direction towards the OAP).

The top right inset in Fig. 1 shows the focal spot profile recorded with the amplified pulse at ~10% of the full laser power attenuated by means of wedges[8]. We have also recorded the full-power focal spot profile using on-shot far-field measurements through a high-reflectivity, high-optical-quality mirror. Both approaches provided fully consistent results. The on-shot pulse spectrum and near-field profiles were also measured using a portion of the beam transmitted through this mirror. The full setup used for spectral measurements (including the mirror, wedges, filters, integrating sphere, fiber, and spectrometer) was absolutely-calibrated using the measured spectrum and the pulse energy after the OAP. We found that the pulse energy determined by integrating this absolutely-calibrated spectrum is more precise than the one obtained from the near-field profile, because the calibration factor of the near-field profile depends on the spectrum of the pulse and, thus, can vary day-to-day and even shot-to-shot.

The temporal laser pulse shape (Fig. 1, bottom inset) with an effective width[8] of 33 fs, was measured with a commercial self-referenced spectral interferometry device (Wizzler)[63] at ~10% of the maximum laser power. In a separate experiment we confirmed that this method gave the same pulse duration as the full-power measurements[64]. The resulting peak intensity in-vacuum was up to $\sim 7\times10^{21}$ W/cm^2. The experiments presented herein were performed in a "medium contrast mode" with a $\sim10^{-10}$ nanosecond laser contrast level, which was optimized for hard X-ray generation. The temporal shape of the prepulse at the nanosecond timescale was also measured on-shot by a fast photodiode. We have performed hydrodynamic simulations, showing

that under our conditions, the preplasma scale length was a few μm and thus did not affect the optimum target position significantly, although it did affect the interaction physics. The small preplasma scale length can be proved indirectly by the fact that the preplasma was not visible on the 2ω interferometer, as it was completely inside the target shadow. Generation of high-order harmonics in the 'specular reflection' direction, which was detected by the 3FF spectrograph and described in Section 7, also indicates a small preplasma scale length. More details on the laser contrast, preplasma, and physics of the hard X-ray generation will be presented elsewhere.

Fig. 1 shows the experimental scheme: the main laser pulse, the 5-to-20-μm-thick stainless steel (SUS) tape target[26] mounted 45º off-normal, and the diagnostics discussed herein:

- (Front) Reflected beam footprint diagnostics (at frequencies 1ω, 2ω and 3ω);
- (Front) Back-reflection diagnostics (at 1ω, the diagnostics is outside Fig. 1);
- (Rear) XUV imaging spectrograph for wavelengths 17 – 25 nm;
- (Rear) Magnetic electron spectrometer (ESM) for 20 – 100 MeV electrons;
- (Rear) Two hard X-ray spectrometers (HXRS-1,2) for 0.1 – 10 MeV photons;
- (Front and Rear) Two soft X-ray focusing spectrometers with spatial resolution (FSSR-F and FSSR-R) for 0.7 – 10 keV photons;
- (Front) Three-channel Flat-Field XUV spectrograph (3FF), λ = 17 – 34 nm.

Here (Front) and (Rear) correspond to the observation on the front and rear sides of the target, respectively. In the latter case, the radiation was going through the target or was generated directly on its rear side.

As EMPs (electromagnetic pulses) from high-power laser-plasma interaction are known to cause troubles to electronics[65], we made attempts to minimize their influence. In previous experiments we tried different motorized platforms from several companies, and finally, we

found that Kohzu Precision can produce custom motorized stages and control electronics highly resistant to EMPs. In particular, these stages were used in our experiments for 3D target translations and rotations. EMPs did not affect our tape movement, as its control system was relatively simple and robust. At the same time, some computers and cameras related to a few diagnostics were affected by the EMPs from time to time, and had to be restarted.

Before each experiment, the initial approximate position of the tape target was determined with a ~100 μm accuracy as follows. We had a focal spot monitor consisting of an apochromatic objective lens and a high-dynamic-range charge coupled device (CCD) camera and set a micro-needle to mark the desired focus position. The needle was positioned by illuminating it with a λ = 785 nm alignment beam (LD7 in Fig. 2 of Ref. [8]) with an axial accuracy of a few μm, limited by the objective depth-of-focus. Then the focal spot quality was measured as described in Ref. [8]. In this process, the OAP was adjusted to bring the focus to the needle position, with a typical axial accuracy of better than ±5 μm, which was around a half of the Rayleigh length. Up to this point, all the steps were implemented with a few-to-several-μm accuracy.

Then a SUS tape target of a 20-mm width was set to the needle position. We tried several methods (see Appendix A), but we were not able to control the target position with a better than 100-μm accuracy, since the SUS target was mirror-like reflective, wrinkle-free, and non-transparent. Finally, we marked the position of the needle on a camera of a 2ω interferometer[66], which observed the target along its 20-mm-long side. After removing the needle, the target orientation was adjusted by the target rotation stage to the narrowest shadow on the 2ω interferometer camera, so the tape was along the probe beam with a ~0.1° accuracy (therefore, the incidence angle was 45°). After that, the target was placed to the needle position with an

accuracy determined by smearing of the tape image along the observation direction, caused by the defocused images of the ±10 mm tape edges, as well as the possible bending of the target edges, that was small in our case on the 100-μm scale, but may be not negligible on the required sub-10-μm scale. From this initial position, the target was shifted by 200 μm towards the OAP (the negative direction in the figures). Then we irradiated the target with high-power laser pulses, performing a target position scan with 10 μm (sometimes 5 μm) steps. We note that shot-to-shot target position variations along the laser axis were less than the depth of focus of the focal-spot monitor objective lens (<2 μm), and the short-term laser pointing stability was ~2-3 μrad, which did not affect the focusing. We stopped the scan after passing the optimum position determined consistently with several X-ray and optical diagnostics. Comparison of the final target position with the initial one determined by the interferometer revealed that the initial target position accuracy was better than ~100 μm.

Hereafter we describe each of the diagnostics listed above (Fig. 1). For convenience, the results of all the diagnostics are given in the same section as their description. The applicability of each instrument for determination of the best *in-focus* target position is discussed.

3. Front-side NIR-vis-UV reflection diagnostics

Several NIR-to-UV diagnostics[67–69] were mounted in the 'specular reflection' direction (90º from the laser incidence direction). Two imaging cameras observed the spatial distributions of 1ω (~700 – 1000 nm) and 2ω (~390 – 410 nm) radiation scattered from a PTFE (Teflon) screen mounted in the 'specular reflection' direction of the laser pulses (see Fig. 1). The spectrum of the reflected beam was measured using the same PTFE screen, with a NIR-vis-UV optical fiber spectrometer (1ω – 4ω) having 200 – 1000 nm total spectral bandwidth.

The fields of view of the two cameras, partially clipped by other instruments, are shown in Fig. 2 (a, b). The acceptance angles were $\Omega_1 \approx 80$ msr and $\Omega_2 \approx 100$ msr for the 1ω and 2ω cameras, respectively. The absolute sensitivity of the 1ω camera together with its filters was calibrated using a small portion of the main laser beam, resulting in $(7.1 \pm 1.5)\times10^{-7}$ J/count. The absolute sensitivity of the spectrometer with a relatively-calibrated spectral response was cross-calibrated with the 1ω camera providing an absolute calibration reference for the whole 200 – 1000 nm spectral region. The 2ω camera was afterwards cross-calibrated with the spectrometer. The area observed with the spectrometer (dashed ellipses in Fig. 2a,b) had an acceptance angle of $\Omega_s \approx 8$ msr. A typical spectrum is shown in Fig. 2c. The absolute energies could be determined for the 1st to 3rd harmonics within the corresponding spectral ranges of $(n \pm 0.25)\cdot\omega_0$, where n is the harmonic order. The spectrometer had low sensitivity in the $\lambda < 200$ nm spectral region, and its sensitivity calibration was unreliable there, as we used two types of commercial calibrated light sources (namely, a black-body source and a deuterium-tungsten halogen lamp) with calibration data given in the spectral range of $\lambda > 200$ nm. Thus, we did not consider the 4th harmonic signal for the target positioning goals.

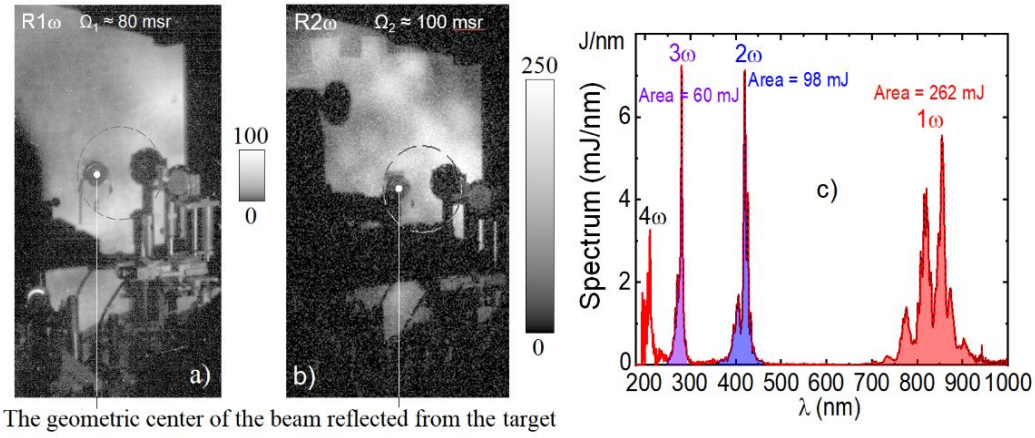

Fig. 2. The fields of view of the 1ω (a) and 2ω (b) cameras imaging a PTFE screen mounted perpendicular to the 'specular reflection' direction. The geometric center of the reflected beam is

marked with the white circles. The dashed ellipses denote the spectrometer observation area. (c) Typical absolutely-calibrated reflected spectrum. The energy values calculated within the $(n \pm 0.25)\cdot\omega_0$ spectral bandwidths (colored) are given for harmonic orders n = 1,2,3.

Along with the 'specular reflection' diagnostics, we also used 1ω back-reflection beam diagnostics. The main purpose of the back-reflection diagnostics is laser safety, as a significant portion of the laser energy can be back-reflected and consequently damage the compressor gratings and/or laser amplifiers. However, this instrument could potentially be useful for determining the best focus position in certain cases.

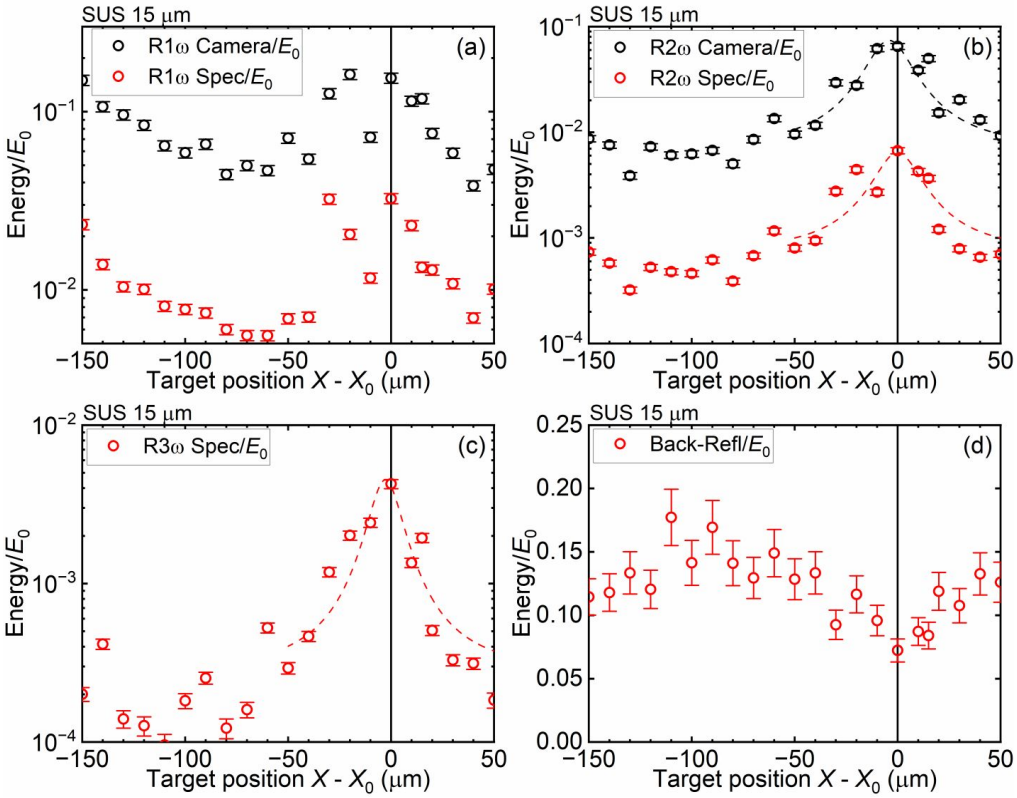

Fig. 3. Normalized energy from the four reflection beam diagnostics versus the target position X ('–' denotes the direction towards the OAP, and X_0 corresponds to the best focus position). All values are normalized by the on-target pulse energy E_0. The plots in (a) and (b) are for the 1ω

and 2ω diagnostics, respectively, where the upper data (black) are from the imagers, while the lower data (red) are integrated from the $1\omega - 4\omega$ spectrometer within $(1 \pm 0.25)\cdot\omega_0$ and $(2 \pm 0.25)\cdot\omega_0$, correspondingly. (c) 3ω data integrated within the $(3 \pm 0.25)\cdot\omega_0$ band from the $1\omega - 4\omega$ spectrometer. (d) shows the normalized back-reflected energy.

Fig. 3 shows the normalized energy (with respect to the total pulse energy *on-target*) detected with all the NIR-vis-UV reflection diagnostics, including the 1ω (a) and 2ω (b) imagers, $1\omega - 4\omega$ spectrometer (a-c) and the 1ω back-reflection (d), recorded for scanned target position. Here X_0 stands for the best focus position, which was consistently determined by multiple diagnostics for each SUS thickness, as described in detail in Section IX. Thus, $X - X_0$ denotes the SUS target displacement from the best focus position.

Fig 3a shows normalized energy determined from the 1ω 'specular reflection' diagnostics, both the 1ω imager and spectrometer signal within the $(1 \pm 0.25)\cdot\omega_0$ band. The data from both instruments were in good correlation. There was a double-peak structure in the vicinity of the best focus and a gradual signal increase from both diagnostics towards $X - X_0 \sim -$ 150 μm, as the interaction probably entered the highly reflective plasma mirror regime. These multi-peak features made the 1ω diagnostics not useful for determination of the best target position.

Fig. 3b shows the dependence of the 2ω normalized energy on $X - X_0$, determined from the 2ω imager (upper points) and spectrometer signal within the $(2 \pm 0.25)\cdot\omega_0$ band (lower points). Both cases reveal single-peak structures that can be approximated with Lorentzian fits, giving the best focus position with ~4 μm discrepancy and 24 μm FWHM, indicating that 2ω 'specular reflection' diagnostics determine the best focus position with a ~12 μm accuracy.

Fig. 3c depicts the energy of the 3ω radiation determined from the 1ω – 4ω spectrometer via integration within the $(3 \pm 0.25)\cdot\omega_0$ spectral band. In the 3ω case, the peak was even more prominent, with small data point fluctuations, indicating a ~5 μm target position accuracy.

Fig. 3d shows the dependence of the normalized back-reflected energy on the relative target position, revealing a broad dip, instead of a peak at the X_0 position, and a broad peak at $X - X_0 \approx -100$ μm. Thus, the 1ω back-reflection, along with other 1ω reflection diagnostics, was not suitable for determination of the best focus position.

4. Rear-side extreme ultraviolet spectrograph (XUV) and electron spectrometer (ESM)

Behind the target, three diagnostics were placed: an extreme ultraviolet imaging spectrograph (XUV), an electron spectrometer (ESM), and a hard X-ray spectrometer (HXRS-2). In this section we describe the first two instruments, while HXRS-2 will be discussed in the next section, along with the HXRS-1 diagnostics of the same type.

XUV imaging spectrograph

An extreme ultraviolet imaging spectrograph (XUV) based on a Mo/Si aperiodic multilayer mirror[70–72] (MM) and a transmission diffraction grating was mounted 12º off the laser direction. The XUV acceptance angle was 3.6 msr, corresponding to a ~2º cone half-angle. The operating range, 17 – 25 nm, was defined by the multilayer structure optimized for maximum uniform reflectance in the 12.5 – 25 nm range[73,74] and absorption cutoff at the aluminum $L_{2,3}$ edge at $\lambda \approx 17$ nm in the optical blocking filters. Imaging spectrographs of this type are used in different forms, e. g. in a combination of a MM with a transmission grating[75] or a varied line space (VLS) reflection grating[76,77]. Such XUV spectrographs have been employed in experiments on

coherent soft X-ray generation via frequency upshift of the laser pulse reflected from a relativistic 'flying mirror'[78] and via the BISER mechanism[41].

A spherical aperiodic Mo/Si MM with a radius of curvature of $R = 1000$ mm was mounted in a geometry providing $M \approx 2.1$ spatial magnification. We used two Al-based free-standing absorption filters to block the NIR-vis-UV radiation: the first filter (0.65 μm thick Al) was mounted in front of the mirror and operated in the double-pass regime, and the second filter (Al/Zr multilayer[79], 0.2 μm) in front of the CCD. A free-standing transmission diffraction grating with a groove density of 5000 lines/mm was situated 139 mm from the CCD chip.

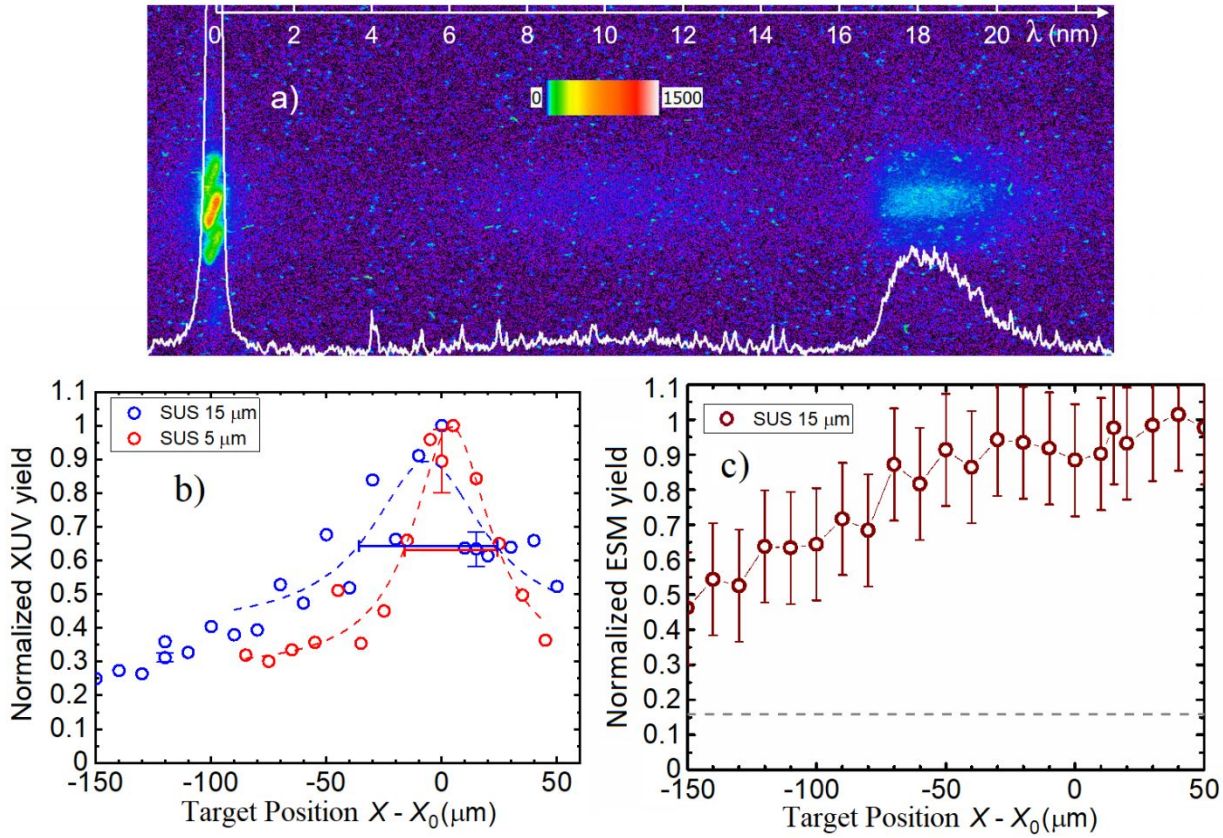

Fig. 4. a) Typical spatially-resolved XUV spectrum; λ = 0 denotes the 0th diffraction order. b) Dependence of the integrated 0th order on the target position ('–' is towards the OAP) for 5-μm and 15-μm-thick targets, and their Lorentzian fits. c) Dependence of the integrated ESM yield on the target position for a 15-μm-thick target. The dashed line shows the ESM noise level.

Fig. 4a shows a typical XUV spectrum for a 5-μm-thick SUS target close to the best focus position (X_0). The XUV spectrum contained the 0th diffraction order and a spectrally-resolved continuous 1st diffraction order in the 17 – 22 nm spectral region. The 0th diffraction order was triple-shaped due to diffraction on the grating support structure, which was perpendicular to the dispersion direction. Each spot in the 0th diffraction order image was elongated due to the astigmatism introduced by the spherical focusing multilayer mirror operating at a small, but non-zero incidence angle. The spectrum decay at $\lambda > 20$ nm was due to absorption of the Al/Zr multilayer filter[79]. Taking the typical CCD spectral sensitivity[80,81] and the spectral filters transmission into account, the total XUV radiation yield on the target rear side was estimated to be ~$(26 \pm 3)\times10^{-10}$ J/sr for the 5-μm-thick, and $(3.8 \pm 0.8)\times10^{-10}$ J/sr for the 15-μm-thick SUS targets, respectively.

The integrated yields in the 0th and the 1st diffraction orders were proportional, with higher signal-to-noise ratio in the 0th order. Fig. 4b gives the dependence of the normalized integrated 0th order signal on $X - X_0$ for 5 μm and 15 μm target thicknesses. Lorentzian-fit curves show that the target thickness affected the precision of the target positioning: 60 μm FWHM for the 15-μm, and a narrower 40 μm FWHM for the 5-μm-thick targets. Deviations of the fitted peaks from the optimal target position were within ~5 μm for both thicknesses, meaning that the XUV imaging spectrograph provided target positioning with a ~20-30 μm accuracy for 5-to-15-μm targets. For 20-μm targets, the XUV signal-to-noise ratio was lower than unity, so precise target positioning was not achievable. The vertical error bars in Fig. 4b stand solely for statistical errors due to shot-to-shot signal variations.

Electron spectrometer (ESM)

The magnetic electron spectrometer (ESM) was mounted on the laser axis (Fig. 1) 509±1 mm from the target. The spectrometer consisted of a 3-mm-diameter collimator, a 100-mm-long dipole magnet with 0.95 T magnetic field, a 150-mm-long LANEX screen and an optical camera with a camera lens and a green spectral filter. The ESM covered the 20 – 100 MeV energy range.

The dependence of the ESM signal on $X - X_0$ for a 15-μm-thick target is shown in Fig. 4c; similar dependences were observed for all target thicknesses under study. The ESM signal had a broad slopped plateau within ±60 μm from the best focus, with a not-so-pronounced peak at $X = +40$ μm, making this instrument not suitable for precise target positioning.

5. Rear-side hard X-ray spectrometers (HXRS-1, HXRS-2)

Two hard X-ray spectrometers (HXRSs)[82,83] were mounted behind the target (Fig. 1): HXRS-1 was 98º from the laser axis, approximately along the laser electric field direction, 1.7 m from the target, and HXRS-2 was on the laser axis, behind the ESM, 4.2 m from the target.

Each of the two HXRS instruments consisted of a linear X-ray absorption array built of 10 LYSO ($Lu_{1.8}Y_{0.2}SiO_5$) scintillator crystal plates of 2 mm thickness and 10×30 mm^2 area, with 2-mm-thick tungsten filters between each pair of plates from #4 to #9 (the numeration of the plates starts from #0). The fluorescence emitted from the LYSO array was monitored with a CMOS camera. Dipole magnets (Fig. 1) in front of the HXRSs prevented electrons from reaching the instruments. The scintillator sensitivity allowed registering hard X-ray radiation with the photon energies from ~20 keV to ~10 MeV, the best sensitivity being 0.1-2 MeV. The harder X-ray radiation was detected by deeper scintillators with higher numbers in the array. A full description of the HXRS design and data processing is in Ref. [84]. In our setup the plate #9 signal was unreliable as, in addition to the X-rays coming through the other scintillators and

tungsten filters in the array, its response included X-rays reflected from the walls of the experimental area. This did not affect other scintillators due to the surrounding lead shielding.

Fig. 5 presents data from HXRS-1 (top) and HXRS-2 (bottom). The scintillator plate number in the array is shown next to the instrument name. The thicker the target, the stronger the recorded HXRS signal was. Frames (a, d) show typical scintillator plate #0 dependences for both instruments, exemplified by dependences for 10-μm-thick targets. The plots contain multi-peak structures, making this channel not suitable for precise target positioning, though the central peak probably might be attributed to the best target position.

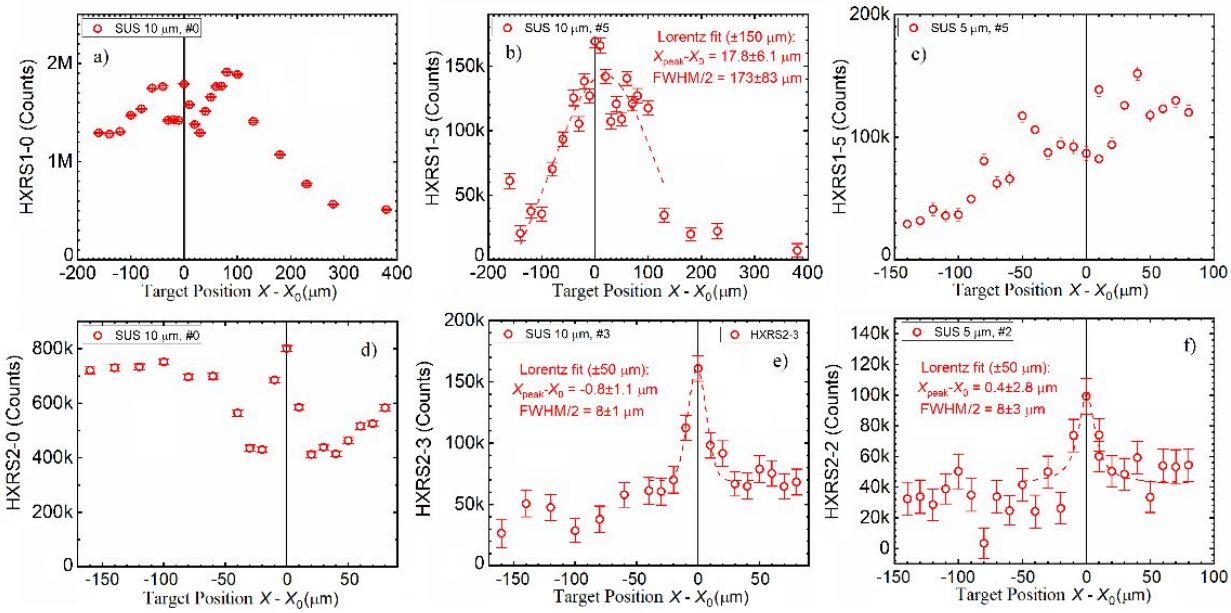

Fig. 5. HXRS scintillator plate signals vs. target position X ('–'is towards the OAP, X_0 is the best focus). (a-c) HXRS-1 (off-axis), (d-f) HXRS-2 (on-axis). a) HXRS-1 plate #0, 10-μm-thick SUS. b) HXRS-1 plate #5, 10-μm-thick SUS. c) HXRS-1 plate #5, 5-μm-thick SUS. d) HXRS-2 plate #0, 10-μm-thick SUS film. e) HXRS-2 plate #3, 10-μm-thick SUS. f) HXRS-2 plate #2, 5-μm-thick SUS. Lorentzian fits are shown, where applicable. Scintillator plate #0 was the closest to the interaction point. The error bars in all the frames are due to the CMOS camera noise.

Frames (b, e) show middle scintillator plate signals for 10-μm-thick targets for HXRS-1 and HXRS-2, respectively. The middle plates were most reliable for thick target positioning due to high signal-to-noise ratios and single peaks in the dependences. There was a narrow peak for the on-axis HXRS-2 (Fig. 5e, 16-μm FWHM fit), and broad peak for the off-axis HXRS-1 (Fig. 5b, >300 μm FWHM). This shows that the target positioning precision was ~5 μm for the on-axis HXRS-2, while it was >100 μm for the off-axis HXRS-1.

Even with the thinnest 5-μm SUS target, the on-axis HXRS-2 middle scintillators were still capable of positioning the target with a ~5 μm accuracy (Fig. 5f), although with a lower signal-to-noise ratio than for thicker targets. The off-axis HXRS-1 middle scintillators were not applicable for determining the best *in-focus* position of 5-μm targets (Fig. 5c).

6. Front-side and rear-side soft X-ray spectrometers with spatial resolution

Two soft X-ray focusing spectrometers with spatial resolution (FSSR) have been assembled on both the front (FSSR-F) and rear (FSSR-R) target sides. The FSSRs were based on spherically-bent mica and quartz crystals, respectively ($2d$ = 2.36 Å in the latter case) with a curvature radius of R = 150 mm to ensure radiation focusing and high spectral resolution, up to a ~10^4 value[85–87].

The FSSR spectrometers were mounted out-of-plane, 786 mm and 819 mm above the horizontal plane containing the laser axis for the FSSR-F and FSSR-R instruments, respectively. FSSR-F was mounted at an in-plane angle of 8.5° ± 0.1° from the target normal and an out-of-plane angle of 17.6° ± 0.1°, with a distance from the FSSR-F crystal to the interaction point of 2600 mm. The mica crystal employed in FSSR-F gave a resolving power of $\lambda/\Delta\lambda \sim 2500$ at the

central wavelength of $\lambda_0 = 0.1875$ nm in the $m = 8$ diffraction order corresponding to a wavelength of 1.5 nm in the first diffraction order.

FSSR-R was mounted at an in-plane angle of 10.1° ± 0.1° from the target normal and an out-of-plane angle of 23.1° ± 0.1°. The quartz crystal provided $\lambda/\Delta\lambda \sim 3000$ resolving power at a wavelength of $\lambda_0 = 0.1812$ nm in the $m = 8$ diffraction order, corresponding to $\lambda = 1.45$ nm in the first diffraction order. The distance from the FSSR-R crystal to the interaction point was 2045 mm.

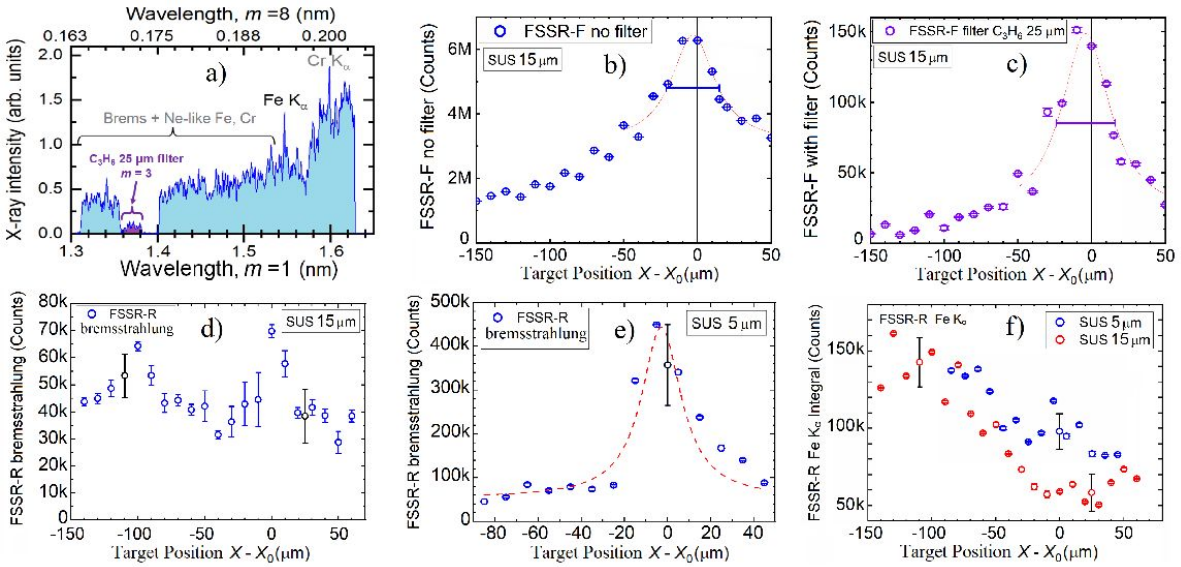

Fig. 6. a) A typical FSSR-F spectrum recorded in the vicinity of the best in-focus target position. The spectrum covers wavelengths from 0.165 nm to 1.63 nm in different diffraction orders from $m = 1$ to $m = 8$. Strong characteristic lines Fe K_α ($\lambda = 0.194$ nm) and Cr K_α ($\lambda = 0.229$ nm) were observed in $m = 8$ and $m = 7$ diffraction orders, respectively. The continuous signal corresponds to bremsstrahlung. A narrow strip of a 25-μm C_3H_6 filter allows observing a narrow portion of the spectrum, suppressing emission from lower diffraction orders ($m = 1$, $m = 2$). (b, c) FSSR-F data for 15-μm SUS targets, integrated within an area without (b) and with (c) the 25-μm-thick C_3H_6 filter. (d, e) FSSR-R integrated bremsstrahlung signal for 15-μm (d) and 5-μm (e) SUS

targets. f) FSSR-R Fe K_α integrated signals for 15-μm and 5-μm SUS targets. The black error bars correspond to statistical shot-to-shot signal variations, while the smaller colored error bars are due to CCD camera noise. Lorentzian fits are shown, where applicable.

An example of the spectrum registered with FSSR-F is shown in Fig. 6a. The spectrum covered a 1.31 – 1.63 nm range of wavelengths in the 1st diffraction order. In this spectrum, the spectral components of the other diffraction orders overlapped, thus making it possible to observe Fe K_α ($\lambda = 0.194$ nm) in the $m = 8$ diffraction order, and Cr K_α ($\lambda = 0.229$ nm) in the $m = 7$ diffraction order. Most of the signals registered with the FSSR-F and FSSR-R detectors in the vicinity of the best *in-focus* target position was bremsstrahlung emitted from the laser-solid interaction. Spectral filters composed of 2-μm-thick C_3H_6 and 0.4-μm Al were placed in front of the CCD camera for the FSSR instruments. An additional narrow strip of a 25-μm-thick C_3H_6 as a spectral filter allowed suppressing $m = 1$ and $m = 2$ diffraction orders and thus catching the bremsstrahlung radiation in the $m = 3$ diffraction order.

Fig. 6 (b-f) give the FSSR-F and FSSR-R data. Panels (b, c) show the FSSR-F spectrally-integrated signals without a spectral filter (which was a sum of the two regions with blue shading in Fig. 6a) and with the 25-μm C_3H_6 spectral filter (with violet shading in Fig. 6a), respectively, for the 15-μm SUS target. A clear ~40-μm FWHM single peak occurs in both cases, assuring the best *in-focus* target positioning with a better than ~20 μm accuracy.

Fig.6 (d, e) show spectrally-integrated bremsstrahlung signals (in the 1.35 – 1.54 nm spectral region in the 1st order of diffraction) from FSSR-R for 15-μm and 5-μm thick targets, respectively. A multi-peak behavior was observed for the 15-μm target (Fig 6d), with one of the peaks (~20 μm FWHM) corresponding to the best *in-focus* target position. The second peak can

be explained by the fact that soft X-rays can be effectively generated from large-area spots at a relatively low intensity. Since the distance between the peaks was ~100 μm, this can give a ~10 μm accuracy, if the target is put within a ~50 μm range from the best-focus position using other diagnostics.

Fig.6f shows dependences of the Fe K_α signals integrated in the 0.1925 – 0.1942 nm spectral region in the 8th diffraction order, on $X - X_0$ for the 15-μm and 5-μm thick SUS targets. Contrary to the previous cases, the Fe K_α signals increased when the target moved away from the best focus. Thus, the Fe K_α line was not suitable for the target positioning.

7. Three-channel flat-field spectrograph (3FF)

The three-channel flat-field (3FF) grazing-incidence spectrograph[88] was mounted in the 'specular reflection' direction behind a hole in the screen used for the NIR-vis-UV diagnostics. The 3FF is a slit-less version of a flat-field spectrograph employing a VLS grating operating at a grazing incidence angle of 4.2º (i. e., 85.8º off-normal), designed for recording a broad spectral region of 5–90 nm[88–90]. For higher spatial resolution and signal-to-noise ratio, three gold-coated grazing-incidence mirrors having shapes of elliptical cylinders were employed. The horizontal acceptance angles were slightly different for the three channels: 0.15º for the shallow-angle mirror, 0.20º for the central mirror, and 0.26º for the high-deviation-angle mirror.

The VLS grating manufactured by Hitachi on a spherical substrate with $R = 5649$ mm had an average central groove density of 1200 lines/mm. The vertical acceptance angle of 0.087º was defined by the $r = 2425$ mm distance from the source to the center of the VLS grating, and by the 50 × 30 mm^2 grating aperture. Thus, the acceptance angles for the three channels were 3.9×10^{-6}, 5.2×10^{-6} and 7.0×10^{-6} sr, respectively. A single-pass 0.65-μm-thick Al filter was mounted in front of the 3FF spectrometer, defining the 17 – 34 nm operating spectral range.

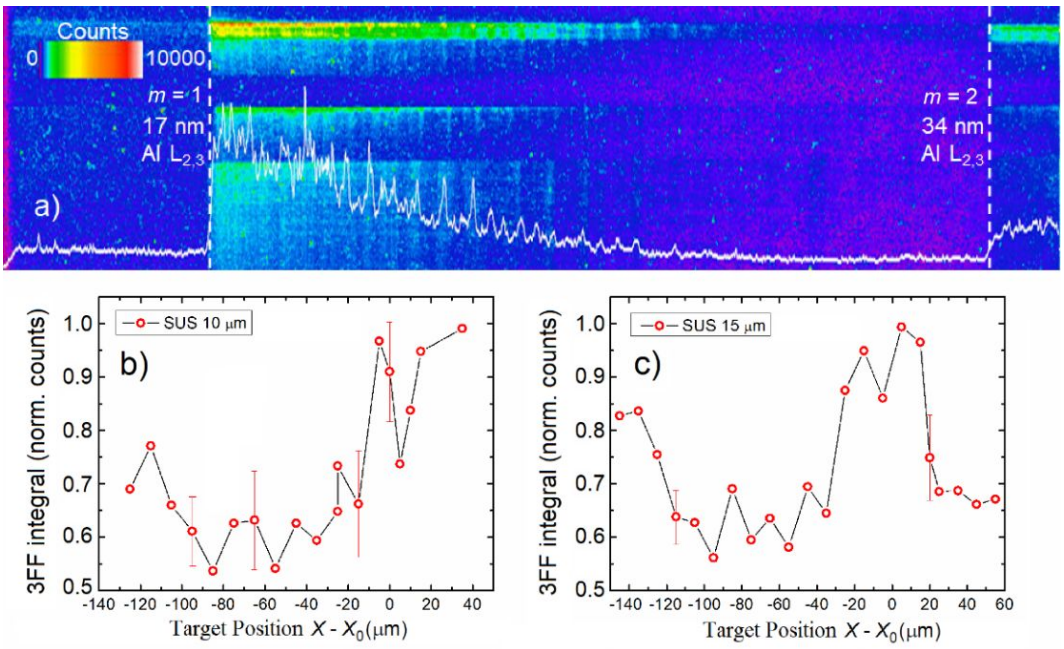

Fig. 7. a) 3FF spectrum with harmonics. The upper and lower parts correspond to the shallow- and high-deviation-angle mirrors, respectively. Dashed lines show the Al filter cutoff (λ = 17 nm) in the 1st and 2nd diffraction orders. (b, c): integrated 3FF signal vs. target position for 10-μm and 15-μm SUS targets, respectively. The error bars correspond to shot-to-shot signal variations.

It is well known that relativistic laser-solid interaction is an intense source of high-order harmonics (HOH) generated mostly in the 'specular reflection' direction[91,92]. However, since the harmonics' divergence can be narrow, we did not observe them in many shots, partly due to the small acceptance angles. Also, HOH generation depends on the pre-plasma scale length[93,94] and intensity, defined in our case by the laser contrast and $X - X_0$ shift.

Fig. 7a shows a typical 3FF spectrum with high-order harmonics. Fig. 7 (b, c) show the dependences of the 3FF signal vs. $X - X_0$ for 10-μm and 15-μm thick SUS targets, respectively. The 3FF data had a ~50 μm broad peak in the vicinity of the best focus, with a clear dip of the

signal near the middle. There was a lower peak at $X - X_0 \sim 120–140$ μm. Within the main 3FF peak, the estimated dimensionless amplitude a_0 was greater than ~10, reaching ~60 at focus. Therefore, the main HOH generation mechanism was the relativistic oscillating mirror[95,96].

We did not observe harmonics in many shots, probably due to the small acceptance angles. Along with this, the optimum combination of the laser intensity and the plasma scale-length might not be satisfied in every shot. The presence of the HOH had been recorded within the ~±25 μm distance from the best *in-focus* target position only, while the relative difference in the integrated signals from the shots with and without harmonics was around ~20%.

Thus, the 3FF spectrometer can determine the best *in-focus* target position with a ~25 μm accuracy, using both the integrated 3FF signal and visual observation of harmonics. The dip in the 3FF signal close to the best focus position X_0 can be used to place the targets with a ~5 μm accuracy, although this result may be laser-contrast-dependent.

8. Discussion

As the laser was operated at a relatively low repetition rate of 0.1 Hz, we wanted to minimize the time spent on the search for the best target position. We used typically 10-to-20 shots during 3 to 11 minutes for the scans presented here, where the latter time was due to manual analysis of readings from many instruments operating simultaneously. All the data acquisition and saving procedures were automated, including automatic file naming with the shot number, for both facility instruments and our metrology. Further, our software automatically indicated the number of counts within our regions of interest. However, the software did not automatically plot the data vs. target position figures. This was done in a separate figure plotting software, which typically took us extra 2-3 minutes for each target thickness. Obviously, this can be automated to speed up the process.

With only 2 or 3 instruments best suited for the target positioning, this time can be reduced down to 1.5–3 minutes with the same laser repetition rate. Our goal was to place the target with an accuracy of better than $\pm Z_R$, where $Z_R \approx 10$ μm is the Rayleigh length. We used 10 μm steps (sometimes 5 μm steps), so that the best *near-focus* target positions were within ±5.0 μm (or ±2.5 μm) from the 'perfect' position. Therefore, even in the worst case, the peak intensity *on-target* was higher than 0.8 (0.94) of the ideal estimated peak value of 7×10^{21} W/cm^2. Assuming random defocusing within the ±5 μm and ±2.5 μm ranges, the intensity was 0.93±0.06 and 0.98±0.02 of the ideal value, respectively.

Table 1. Accuracy of the instruments for the best *in-focus* target positioning.

Name of the instrument	**Peak FWHM, μm**	**Peak shift, μm**	**Estimated* accuracy, μm**	**Comment**
Reflection 'specular direction' camera, 1ω	~60	~20	~30	Multi-peak
Reflection 'specular direction' camera, 2ω	24 ± 6	<5	~12	
Reflection 'specular direction' spectrometer, 1ω	~70	~30	~30	Multi-peak
Reflection 'specular direction' spectrometer, 2ω	24 ± 10	<5	~12	
Reflection 'specular direction' spectrometer, 3ω	18 ± 6	<4	~5	
Back-reflection camera	Not applicable			No peak
Rear-Side XUV – thin targets	40 ± 6	<5	~20	
Rear-Side XUV – thick targets	60 ± 26	<10	~30	Weak signal

Rear-Side ESM	~120	~40	~60	Plateau-like
Rear-Side HXRS-1 (off-axis) – thin targets	~120	~50	~60	No clear peak
Rear-Side HXRS-1 (off-axis) – thick targets	~200	~20	~100	Broad peak
Rear-Side HXRS-2 (on-axis) – thin targets	16 ± 6	<4	~5	Weak signal
Rear-Side HXRS-2 (on-axis) – thick targets	16 ± 2	<2.5	~5	
Front-Side FSSR-F	40 ± 10	<5	~20	
Rear-Side FSSR-R – bremsstrahlung integral	24 ± 8	<5	~12	Double-peak
Rear-Side FSSR-R – Fe K_α integral	Not applicable			Multi-peak
'Specular reflection' 3FF spectrometer – integral	~50	~10	~25	Multi-peak
'Specular reflection' 3FF spectrometer – HOH	~50	~10	~25	
'Specular reflection' 3FF spectrometer – central dip	~10	~5	~5	Contrast-dependent

*Estimated accuracy was a half-step size for the clean peaks, and a half-width at half-maximum (HWHM) for instruments with notable data fluctuations.

In Table 1 we summarize all the information presented in the previous sections. In most cases our scans were single-shot at each position, and the accuracy was estimated for this approach. The main limiting factors were shot-to-shot fluctuations and available experimental time. By multi-shot averaging, one can reduce the influence of the shot-to-shot fluctuations.

The best target positioning accuracy of ~5 μm was achieved using on-axis HXRS-2 inner scintillators and the third order harmonic (3ω) instrument mounted in the 'specular reflection' direction. The 2ω, FSSR-F, FSSR-R, 3FF and XUV diagnostics provided an accuracy of ~10 to 20 μm. The instruments that suited the best for the precise target positioning goals, had peaks with good symmetrical shape and low data fluctuations, which means that the accuracy was better than HWHM and corresponded to half-step of the scanning. On the other hand, if the data fluctuations are high enough, then the accuracy should be estimated as HWHM of the fitted peak.

Several diagnostics, such as 1ω reflection, ESM, low X-ray photon energy plates #0 of HXRS-1,2, and Fe K_α yield were not suitable for determination of the best target position, since their highest signals were reached from out-of-focus large-area low-intensity interactions.

In this paper, we presented the diagnostics as useful means to find the best target position. If the main purpose of an experiment is hard X-ray generation, then our optimization with the HXRS-2 spectrometer immediately provides the best target position. At the same time, all our selected diagnostics operating at the target front and rear sides, in optical, XUV, and X-ray regions, provided the same best target positions, as the hard X-ray (MeV) diagnostic, within their respective accuracy limits. And this was proved for each of the target thicknesses tested. Considering a small (a few μm) preplasma length, it is unlikely that some other point in space, rather than the focus, would give a maximum for all the so diverse diagnostics simultaneously. Thus, we conclude that the targets were placed to the best focus position.

Let us mention that we have investigated signals from many diagnostics, while most of the instruments we used in our study, are not necessary at many high-power-laser facilities for the goal of the best target positioning. In experiments similar to ours, given specific space

constraints, an experimental team can choose 2-3 reliable diagnostics from the set described herein, and this should be enough for the precise target positioning. Furthermore, we anticipate that placing some of the instruments at similar, but not exactly the same positions as described in this paper, using slightly different in-plane and out-of-plane angles, one can obtain similar results for the best target positioning purpose. However, this has to be proved in a separate dedicated study.

As for the types of targets that can be precisely placed to the best focus position using our method, we can highlight three important requirements:

1) The target must be reproducibly positioned with a few-μm accuracy;

2) The positioning of the target before each shot should be fast, ideally, faster than the laser system inverse repetition rate (for slower target positioning systems, the procedure becomes correspondingly longer; in case of very long shot-to-shot intervals, the thermal laser stability on the extended time periods should be also tested and controlled);

3) The targets used for the position scan should be identical or almost identical to keep the diagnostics output consistent (after that, other target types can be used, if placement to the same position is guaranteed).

We expect that any kind of target that complies with these three requirements, can be precisely placed to the best focus position using our method. From our point of view, tape targets are the best for this purpose. Liquid targets can also be feasible. With the abovementioned restrictions, thin foils and nanostructured targets can also be used.

Compared to the well-established methods[45–47], our proposed technique does not need coincidence or calculatable difference[97,98] between the positions of low-power and high-power focal planes. Furthermore, as the main experimental data shots immediately follow the focusing

scan without changing the laser mode, moving instruments in and out, or replacing filters in the laser diagnostics, the influence of long-term instabilities and thermal drifts was minimized. At the same time, our method relies on shot-to-shot reproducible laser parameters and the target position, which is relatively easily achievable with high-repetition-rate lasers and tape targets, while it can be challenging for less stable lasers or other target supply systems.

9. Conclusions

We have investigated the usefulness of eleven diagnostics (Table 1) for the best *in-focus* target positioning in order to have the highest *on-target* laser intensity in a relativistic laser-solid interaction experiment. The main challenge was to put the solid target within an extremely short Rayleigh length of ~10 μm. We found that several diagnostics can ensure this accuracy.

The sharpest and most reliable diagnostic instrument was the rear-side on-axis hard X-ray spectrometer HXRS-2 made of ten LYSO scintillator crystal plates with the best sensitivity of the inner crystals to the radiation energy of 0.1-2 MeV[82,83]. The prominent and clean signal maxima allowed us to find the best *in-focus* target position with an accuracy of better than 5 μm, determined by a half step size during the target position scan.

Several other instruments were also capable of positioning the target within a comparable accuracy of ~5–10 μm. They were low-order harmonics (2ω, 3ω) mounted in the 'specular reflection' direction[67–69]. At 2ω, a camera and fiber spectrometer provided consistent results.

The integrated bremsstrahlung signal over the 0.7 – 10 keV range (but *not* the K_α radiation) recorded with the rear-side FSSR-R spectrometer could also give a ~10 μm accuracy. However, the FSSR-R data had a double-peak shape with peak separation of ~100 μm, requiring a correct peak selection by means of other diagnostics. The front-side FSSR-F accuracy was ~20 μm.

The rear-side XUV spectrometer (λ = 17 – 22 nm) provided ~20 μm accuracy for ≤10 μm targets. For 15-μm targets, the signal-to-noise ratio became low, and the peak width increased, so the accuracy was around ~30 μm. For 20-μm targets, XUV diagnostics was not applicable.

The 'specular reflection' 3FF spectrograph (17 – 34 nm) showed a multi-peak dependence, with ~30% probability of high-order harmonics registration within ±25 μm from the best focus. If the correct peak was picked by means of other diagnostics, the 3FF provided ~25 μm target positioning accuracy. The central peak in the dependency had a dip at the best focus position for all target thicknesses, suggesting a better, ~5 μm accuracy (though it may be contrast-dependent).

All front-side 1ω diagnostics, as well as the rear-side electron spectrometer (ESM) and off-axis HXRS-1 hard X-ray spectrometer, were not applicable for target positioning, because the estimated precision of those instruments was worse than ~30 μm. We note that some of these might be used as auxiliary diagnostics to roughly put the target with a ~30 – 100 μm accuracy.

Employing the best diagnostics, we consistently performed the best *in-focus* target positioning with an estimated accuracy of ~5 μm and discrepancy <5 μm between many instruments, resulting in the intensity *on-target* of at least 80% (94% for some scans) of the ideal estimate of 7×10^{21} W/cm^2.

Acknowledgements

We acknowledge financial support from ELI-Beamlines, project Advanced Research using High Intensity Laser Produced Photons and Particles (ADONIS) (Project No. CZ.02.1.01/0.0/0.0/16_019/0000789) from the European Regional Development Fund, QST-IRI, QST President's Strategic Grant (Creative Research), and JSPS KAKENHI JP17F17811, JP19KK0355, JP19H00669 and JP22H01239. Authors' thanks also go to the Czech Ministry of

Education, Youth and Sports (CMEYS) for the financial support of the project number LM2023068.

We thank the J-KAREN-P operation group. The on-target pulse energy measurement from absolutely-calibrated spectrometer was performed in collaboration with M. Nishiuchi and N. Dover. We highly appreciate the contribution of professor David Neely who sadly passed away before this work was published; he was a colleague, mentor, and friend to the authors. This work supports the ongoing diagnostic development research at the Central Laser Facility and is supported by the EPAC diagnostic work package.

Appendix A

Here we describe the target positioning methods that we have tried, but found out that they cannot provide the required ~10 μm accuracy.

1. **Imaging the target surface with a focal spot monitor.** This method is often used with transparent targets using the attenuated defocused laser beam transmitted through the target. However, in our case of non-transparent stainless-steel tapes it was not usable. A variation of this method with white-lite illumination from the rear side of the target required significant light power, due to the high imaging system magnification, which led to the target heating and notable bending, which we confirmed by varying the illumination light power. We note that the thermal bending problem can be avoided by using a confocal microscope, which requires much lower light power, however, we did not have this technique as a facility device and decided not to implement it as a part of our experiment, because, even though this device might really help us precisely position the target to a plane coincident with the focal plane of the low-power laser beam in a mode used for the alignment, this does not guarantee that the full-power-mode beam would have focus at the same plane with the required sub-10-μm accuracy.

2. **Imaging the edge of the non-transparent target with a focal spot monitor.** This method is often used with relatively narrow targets, when the possible errors in the target translation direction do not lead to significant defocusing. However, in our case of 20-mm-wide tapes, the direction error in the target translation by a distance of 10 mm could lead to a substantial target position mismatch. We note that narrower tapes could not be used in our case, as this increased significantly the frequency of the tape breaking under the exposure to the full-power shots, as we experienced in previous experiments. Also, any possible target edge bending may cause additional positioning errors. And the final reason was the same, as in the previous method. Even though the technical difficulties of this method can be potentially overcome, the target would be positioned to the low-power-mode focal plane, which is not necessarily the same as for the high-power beam.

As a summary, we state that the methods described in this Appendix can be used for the initial target positioning with a ~100 μm accuracy before the experiment. Our choice of pre-positioning the target using the interferometry line, as described in the main text, was a matter of convenience, because it also ensured alignment of the target rotation angle with a ~0.1° accuracy.

References

1. D. Strickland and G. Mourou, "Compression of amplified chirped optical pulses," Opt. Commun. **56**, 219 (1985).
2. A. V. Mitrofanov, A. A. Voronin, D. A. Sidorov-Biryukov, S. I. Mitryukovsky, A. B. Fedotov, E. E. Serebryannikov, D. V. Meshchankin, V. Shumakova, S. Ališauskas, A. Pugžlys, V. Ya. Panchenko, A. Baltuška, and A. M. Zheltikov, "Subterawatt few-cycle mid-infrared pulses from a single filament," Optica **3**, 299 (2016).
3. V. V. Lozhkarev, G. I. Freidman, V. N. Ginzburg, E. V. Katin, E. A. Khazanov, A. V. Kirsanov, G. A. Luchinin, A. N. Mal'shakov, M. A. Martyanov, O. V. Palashov, A. K.

Poteomkin, A. M. Sergeev, A. A. Shaykin, and I. V. Yakovlev, "Compact 0.56 Petawatt laser system based on optical parametric chirped pulse amplification in KD*P crystals," Laser Phys. Lett. **4**, 421 (2007).

4. V. Yanovsky, V. Chvykov, G. Kalinchenko, P. Rousseau, T. Planchon, T. Matsuoka, A. Maksimchuk, J. Nees, G. Cheriaux, G. Mourou, and K. Krushelnick, "Ultra-high intensity- 300-TW laser at 0.1 Hz repetition rate," Opt. Express **16**, 2109 (2008).
5. Z.-J. Ren, X.-Y. Liang, L.-H. Yu, X.-M. Lu, Y.-X. Leng, R.-X. Li, and Z.-Z. Xu, "Efficient Spherical Wavefront Correction near the Focus for the 0.89 PW/29.0 fs Ti:Sapphire Laser Beam," Chin. Phys. Lett. **28**, 024201 (2011).
6. P. L. Poole, C. Willis, R. L. Daskalova, K. M. George, S. Feister, S. Jiang, J. Snyder, J. Marketon, D. W. Schumacher, K. U. Akli, L. Van Woerkom, R. R. Freeman, and E. A. Chowdhury, "Experimental capabilities of 0.4 PW, 1 shot/min Scarlet laser facility for high energy density science," Appl. Opt. **55**, 4713 (2016).
7. H. Kiriyama, M. Mori, A. S. Pirozhkov, K. Ogura, A. Sagisaka, A. Kon, T. Z. Esirkepov, Y. Hayashi, H. Kotaki, M. Kanasaki, H. Sakaki, Y. Fukuda, J. Koga, M. Nishiuchi, M. Kando, S. V. Bulanov, K. Kondo, P. R. Bolton, O. Slezak, D. Vojna, M. Sawicka-Chyla, V. Jambunathan, A. Lucianetti, and T. Mocek, "High-Contrast, High-Intensity Petawatt-Class Laser and Applications," IEEE J. Sel. Top. Quantum Electron. **21**, 1601118 (2015).
8. A. S. Pirozhkov, Y. Fukuda, M. Nishiuchi, H. Kiriyama, A. Sagisaka, K. Ogura, M. Mori, M. Kishimoto, H. Sakaki, N. P. Dover, K. Kondo, N. Nakanii, K. Huang, M. Kanasaki, and M. Kando, "Approaching the diffraction-limited, bandwidth-limited Petawatt," Opt. Express **25**, 20486 (2017).
9. S. V. Alekseev, M. V. Ivanov, N. G. Ivanov, V. F. Losev, G. A. Mesyats, L. D. Mikheev, Yu. N. Panchenko, N. A. Ratakhin, and A. G. Yastremskii, "THL-100 Multi-Terawatt Laser System of Visible Range," Russ. Phys. J. **60**, 1346 (2017).
10. S. V. Alekseev, N. G. Ivanov, V. F. Losev, G. A. Mesyats, L. D. Mikheev, N. A. Ratakhin, and Yu. N. Panchenko, "THL-100 multi-terawatt laser system of visible spectrum range," Opt. Commun. **455**, 124386 (2020).
11. M. R. Edwards, N. M. Fasano, T. Bennett, A. Griffith, N. Turley, B. M. O'Brien, and J. M. Mikhailova, "A multi-terawatt two-color beam for high-power field-controlled nonlinear optics," Opt. Lett. **45**, 6542 (2020).

12. P. Panagiotopoulos, M. G. Hastings, M. Kolesik, S. Tochitsky, and J. V. Moloney, "Multi-terawatt femtosecond 10 μm laser pulses by self-compression in a CO2 cell," OSA Contin. **3**, 3040, (2020).
13. T. M. Jeong and J. Lee, "Femtosecond petawatt laser," Annalen der Physik **526**, 157 (2014).
14. C. J. Hooker, S. Blake, O. Chekhlov, R. J. Clarke, J. L. Collier, E. J. Divall, K. Ertel, P. S. Foster, S. J. Hawkes, P. Holligan, B. Landowski, B. J. Lester, D. Neely, B. Parry, R. Pattathil, M. Streeter, and B. E. Wyborn, "Commissioning the Astra Gemini Petawatt Ti:Sapphire Laser System," in *CLEO* (OSA Technical Digest, 2008), paper JThB2.
15. T. J. Yu, S. K. Lee, J. H. Sung, J. W. Yoon, T. M. Jeong, and J. Lee, "Generation of high-contrast, 30 fs, 1.5 PW laser pulses from chirped-pulse amplification Ti:sapphire laser," Opt. Express **20**, 10807 (2012).
16. W. P. Leemans, J. Daniels, A. Deshmukh, A. J. Gonsalves, A. Magana, H. S. Mao, D. E. Mittelberger, K. Nakamura, J. R. Riley, and D. Syversrud, "BELLA laser and operations," in *Proc. PAC* (2013), p. 1097–1100.
17. J. H. Sung, H. W. Lee, J. Y. Yoo, J. W. Yoon, C. W. Lee, J. M. Yang, Y. J. Son, Y. H. Jang, S. K. Lee, and C. H. Nam, "4.2 PW, 20 fs Ti:sapphire laser at 0.1 Hz," Opt. Lett. **42**, 2058 (2017).
18. W. Li, Z. Gan, L. Yu, C. Wang, Y. Liu, Z. Guo, L. Xu, M. Xu, Y. Hang, J. Xu, J. Wang, P. Huang, H. Cao, B. Yao, X. Zhang, L. Chen, Y. Tang, S. Li, X. Liu, S. Li, M. He, D. Yin, X. Liang, Y. Leng, R. Li, and Z. Xu, "339 J high-energy Ti:sapphire chirped-pulse amplifier for 10 PW laser facility," Opt. Lett. **43**, 5681 (2018).
19. F. Lureau, O. Chalus, G. Matras, S. Laux, C. Radier, O. Casagrande, C. Derycke, S. Ricaud, G. Rey, T. Morbieu, A. Pellegrina, L. Boudjemaa, C. Simon-Boisson, A. Baleanu, R. Banici, A. Gradinariu, C. Caldararu, P. Ghenuche, A. Naziru, G. Kolliopoulos, L. Neagu, B. De Boisdeffre, D. Ursescu, and I. Dancus, "10 petawatt lasers for extreme light applications," Proc. SPIE **11259**, Solid State Lasers XXIX: Technology and Devices, 112591J (2020).
20. F. Lureau, G. Matras, O. Chalus, C. Derycke, T. Morbieu, C. Radier, O. Casagrande, S. Laux, S. Ricaud, G. Rey, A. Pellegrina, C. Richard, L. Boudjemaa, C. Simon-Boisson, A. Baleanu, R. Banici, A. Gradinariu, C. Caldararu, B. De Boisdeffre, P. Ghenuche, A.

Naziru, G. Kolliopoulos, L. Neagu, R. Dabu, I. Dancus, and D. Ursescu, "High-energy hybrid femtosecond laser system demonstrating 2×10 PW capability," High Power Laser Sci. Eng. **8**, e43 (2020).

21. I. V. Yakovlev, "Stretchers and compressors for ultra-high power laser systems," Quantum Electron. **44**, 393 (2014).
22. C. Danson, D. Hillier, N. Hopps, and D. Neely, "Petawatt class lasers worldwide," High Power Laser Sci. Eng. **3**, e3 (2015).
23. C. N. Danson, C. Haefner, J. Bromage, T. Butcher, J.-C. F. Chanteloup, E. A. Chowdhury, A. Galvanauskas, L. A. Gizzi, J. Hein, D. I. Hillier, N. W. Hopps, Y. Kato, E. A. Khazanov, R. Kodama, G. Korn, R. Li, Y. Li, J. Limpert, J. Ma, C. H. Nam, D. Neely, D. Papadopoulos, R. R. Penman, L. Qian, J. J. Rocca, A. A. Shaykin, C. W. Siders, C. Spindloe, S. Szatmári, R. M. G. M. Trines, J. Zhu, P. Zhu, and J. D. Zuegel, "Petawatt and exawatt class lasers worldwide," High Power Laser Sci. Eng. **7**, e54 (2019).
24. G. A. Mourou, T. Tajima, and S. V. Bulanov, "Optics in the relativistic regime," Rev. Mod. Phys. **78**, 309 (2006).
25. M. Nishiuchi, N. P. Dover, M. Hata, H. Sakaki, Ko. Kondo, H. F. Lowe, T. Miyahara, H. Kiriyama, J. K. Koga, N. Iwata, M. A. Alkhimova, A. S. Pirozhkov, A. Ya. Faenov, T. A. Pikuz, A. Sagisaka, Y. Watanabe, M. Kando, K. Kondo, E. J. Ditter, O. C. Ettlinger, G. S. Hicks, Z. Najmudin, T. Ziegler, K. Zeil, U. Schramm, and Y. Sentoku, "Dynamics of laser-driven heavy-ion acceleration clarified by ion charge states," Phys. Rev. Res. **2**, 033081 (2020).
26. Ko. Kondo, M. Nishiuchi, H. Sakaki, N. P. Dover, H. F. Lowe, T. Miyahara, Y. Watanabe, T. Ziegler, K. Zeil, U. Schramm, E. J. Ditter, G. S. Hicks, O. C. Ettlinger, Z. Najmudin, H. Kiriyama, M. Kando, and K. Kondo, "High-intensity laser-driven oxygen source from CW laser-heated Titanium tape targets," Crystals **10**, 837 (2020).
27. N. P. Dover, M. Nishiuchi, H. Sakaki, Ko. Kondo, H. F. Lowe, M. A. Alkhimova, E. J. Ditter, O. C. Ettlinger, A. Ya. Faenov, M. Hata, G. S. Hicks, N. Iwata, H. Kiriyama, J. K. Koga, T. Miyahara, Z. Najmudin, T. A. Pikuz, A. S. Pirozhkov, A. Sagisaka, U. Schramm, Y. Sentoku, Y. Watanabe, T. Ziegler, K. Zeil, M. Kando, and K. Kondo, "Demonstration of repetitive energetic proton generation by ultra-intense laser interaction with a tape target," High Intensity Density Phys. **37**, 100847 (2020).

28. N. P. Dover, M. Nishiuchi, H. Sakaki, Ko. Kondo, M. A. Alkhimova, A. Ya. Faenov, M. Hata, N. Iwata, H. Kiriyama, J. K. Koga, T. Miyahara, T. A. Pikuz, A. S. Pirozhkov, A. Sagisaka, Y. Sentoku, Y. Watanabe, M. Kando, and K. Kondo, "Effect of small focus on electron heating and proton acceleration in ultrarelativistic laser-solid interactions," Phys. Rev. Lett. **124**, 084802 (2020).
29. R. Hollinger, S. Wang, Y. Wang, A. Moreau, M. G. Capeluto, H. Song, A. Rockwood, E. Bayarsaikhan, V. Kaymak, A. Pukhov, V. N. Shlyaptsev, and J. J. Rocca, "Extreme ionization of heavy atoms in solid-density plasmas by relativistic second-harmonic laser pulses," Nat. Photon. **14**, 607 (2020).
30. P. Wang, Z. Gong, S. G. Lee, Y. Shou, Y. Geng, C. Jeon, I. J. Kim, H. W. Lee, J. W. Yoon, J. H. Sung, S. K. Lee, D. Kong, J. Liu, Z. Mei, Z. Cao, Z. Pan, I. W. Choi, X. Yan, C. H. Nam, and W. Ma, "Super-heavy ions acceleration driven by ultrashort laser pulses at ultrahigh intensity," Phys. Rev. X **11**, 021049 (2021).
31. A. X. Li, C. Y. Qin, H. Zhang, S. Li, L. L. Fan, Q. S. Wang, T. J. Xu, N. W. Wang, L. H. Yu, Y. Xu, Y. Q. Liu, C. Wang, X. L. Wang, Z. X. Zhang, X. Y. Liu, P. L. Bai, Z. B. Gan, X. B. Zhang, X. B. Wang, C. Fan, Y. J. Sun, Y. H. Tang, B. Yao, X. Y. Liang, Y. X. Leng, B. F. Shen, L. L. Ji, R. X. Li, and Z. Z. Xu, "Acceleration of 60 MeV proton beams in the commissioning experiment of the SULF-10 PW laser," High Power Laser Sci. Eng. **10**, e26 (2022).
32. F. Kroll, F.-E. Brack, C. Bernert, S. Bock, E. Bodenstein, K. Brüchner, T. E. Cowan, L. Gaus, R. Gebhardt, U. Helbig, L. Karsch, T. Kluge, S. Kraft, M. Krause, E. Lessmann, U. Masood, S. Meister, J. Metzkes-Ng, A. Nossula, J. Pawelke, J. Pietzsch, T. Püschel, M. Reimold, M. Rehwald, C. Richter, H.-P. Schlenvoigt, U. Schramm, M. E. P. Umlandt, T. Ziegler, K. Zeil, and E. Beyreuther, "Tumour irradiation in mice with a laser-accelerated proton beam," Nat. Phys. **18**, 316 (2022).
33. C. Bernert, S. Assenbaum, S. Bock, F.-E. Brack, T. E. Cowan, C. B. Curry, M. Garten, L. Gaus, M. Gauthier, R. Gebhardt, S. Göde, S. H. Glenzer, U. Helbig, T. Kluge, S. Kraft, F. Kroll, L. Obst-Huebl, T. Püschel, M. Rehwald, H.-P. Schlenvoigt, C. Schoenwaelder, U. Schramm, F. Treffert, M. Vescovi, T. Ziegler, and K. Zeil, "Transient Laser-Induced Breakdown of Dielectrics in Ultrarelativistic Laser-Solid Interactions," Phys. Rev. Appl. **19**, 014070 (2023).

34. T. Esirkepov, M. Borghesi, S. V. Bulanov, G. Mourou, and T. Tajima, “Highly Efficient Relativistic-Ion Generation in the Laser-Piston Regime,” Phys. Rev. Lett. **92**, 175003 (2004).
35. T. Z. Esirkepov, M. Yamagiwa, and T. Tajima, “Laser ion-acceleration scaling laws seen in multiparametric particle-in-cell simulations,” Phys. Rev. Lett. **96**, 105001 (2006).
36. A. Di Piazza, C. Müller, K. Z. Hatsagortsyan, and C. H. Keitel, “Extremely high-intensity laser interactions with fundamental quantum systems,” Rev. Mod. Phys. **84**, 1177 (2012).
37. S. S. Bulanov, V. D. Mur, N. B. Narozhny, J. Nees, and V. S. Popov, “Multiple colliding electromagnetic pulses: a way to lower the threshold of e^{+} e^{-} pair production from vacuum,” Phys. Rev. Lett. **104**, 220404 (2010).
38. J. W. Yoon, Y. G. Kim, I. W. Choi, J. H. Sung, H. W. Lee, S. K. Lee, and C. H. Nam, “Realization of laser intensity over 10^{23} W/cm^2,” Optica **8**, 630 (2021).
39. K. Nakamura, H.-S. Mao, A. J. Gonsalves, H. Vincenti, D. E. Mittelberger, J. Daniels, A. Magana, Cs. Toth, and W. P. Leemans, “Diagnostics, Control and Performance Parameters for the BELLA High Repetition Rate Petawatt Class Laser,” IEEE J. Quantum Electron. **53**, 1200121 (2017).
40. X. Wang, R. Zgadzaj, N. Fazel, Z. Li, S. A. Yi, X. Zhang, W. Henderson, Y. Y. Chang, R. Korzekwa, H. E. Tsai, C. H. Pai, H. Quevedo, G. Dyer, E. Gaul, M. Martinez, A. C. Bernstein, T. Borger, M. Spinks, M. Donovan, V. Khudik, G. Shvets, T. Ditmire, and M. C. Downer, “Quasi-monoenergetic laser-plasma acceleration of electrons to 2 GeV,” Nat. Commun. **4**, 1988 (2013).
41. A. S. Pirozhkov, T. Z. Esirkepov, T. A. Pikuz, A. Y. Faenov, K. Ogura, Y. Hayashi, H. Kotaki, E. N. Ragozin, D. Neely, H. Kiriyama, J. K. Koga, Y. Fukuda, A. Sagisaka, M. Nishikino, T. Imazono, N. Hasegawa, T. Kawachi, P. R. Bolton, H. Daido, Y. Kato, K. Kondo, S. V. Bulanov, and M. Kando, “Burst intensification by singularity emitting radiation in multi-stream flows,” Sci. Rep. **7**, 17968 (2017).
42. A. S. Pirozhkov, T. Z. Esirkepov, T. A. Pikuz, A. Y. Faenov, A. Sagisaka, K. Ogura, Y. Hayashi, H. Kotaki, E. N. Ragozin, D. Neely, J. K. Koga, Y. Fukuda, M. Nishikino, T. Imazono, N. Hasegawa, T. Kawachi, H. Daido, Y. Kato, S. V. Bulanov, K. Kondo, H. Kiriyama, and M. Kando, “Laser Requirements for High-Order Harmonic Generation by Relativistic Plasma Singularities,” Quantum Beam Sci. **2**, 7 (2018).

43. H. Daido, M. Nishiuchi, and A. S. Pirozhkov, "Review of laser-driven ion sources and their applications," Rep. Prog. Phys. **75**, 056401 (2012).
44. S. Singh, M. Krupka, V. Istokskaia, J. Krasa, L. Guiffrida, R. Dudzak, J. Dostal, T. Burian, R. Versaci, D. Margarone, T. Pisarczyk, M. Krus, and L. Juha, "Hot electron and x-ray generation by sub-ns kJ-class laser-produced tantalum plasma," Plasma Phys. Control. Fusion **64**, 105012 (2022).
45. P. McKenna, K. W. D. Ledingham, I. Spencer, T. McCany, R. P. Singhal, C. Ziener, P. S. Foster, E. J. Divall, C. J. Hooker, D. Neely, A. J. Langley, R. J. Clarke, P. A. Norreys, K. Krushelnick, and E. L. Clark, "Characterization of multiterawatt laser-solid interactions for proton acceleration," Rev. Sci. Instr. **73**, 4176 (2002).
46. I. W. Choi, H. T. Kim, N. Hafz, T. J. Yu, J. H. Sung, K. Lee, C. M. Kim, I. J. Kim, Y.-C. Noh, D.-K. Ko, and J. Lee, "Target Diagnostic Systems for Proton, Electron, and X-ray Generation Experiments Based on Ultraintense Laser-Target Interactions," J. Korean Phys. Soc. **55**, 517 (2009).
47. C. Willis, P. L. Poole, K. U. Akli, D. W. Schumacher, and R. R. Freeman, "A confocal microscope position sensor for micron-scale target alignment in ultra-intense laser-matter experiments," Rev. Sci. Instr. **86**, 053303 (2015).
48. Y. Wang, S. Wang, A. Rockwood, B. M. Luther, R. Hollinger, A. Curtis, C. Calvi, C. S. Menoni, and J. J. Rocca, "0.85 PW laser operation at 3.3 Hz and high-contrast ultrahigh-intensity $\lambda = 400$ nm second-harmonic beamline," Opt. Lett. **42**, 3828 (2017).
49. C. J. Hooker, J. L. Collier, O. Chekhlov, R. J. Clarke, E. J. Divall, K. Ertel, P. Foster, S. Hancock, S. J. Hawkes, P. Holligan, A. J. Langley, W. J. Lester, D. Neely, B. T. Parry, and B. E. Wyborn, "The Astra Gemini Petawatt Ti:Sapphire Laser," Rev. Laser Eng. **37**, 443 (2009).
50. B. Le Garrec, D. N. Papadopoulos, C. Le Blanc, J. P. Zou, G. Chériaux, P. Georges, F. Druon, L. Martin, A. Fréneaux, A. Beluze, N. Lebas, F. Mathieu, and P. Audebert, "Design update and recent results of the Apollon 10 PW facility," Proc. SPIE **10238**, High-Power, High-Energy, and High-Intensity Laser Technology III, 102380Q (2017).
51. A. Kessel, V. E. Leshchenko, O. Jahn, M. Krüger, A. Münzer, A. Schwarz, V. Pervak, M. Trubetskov, S. A. Trushin, F. Krausz, Z. Major, and S. Karsch, "Relativistic few-cycle pulses with high contrast from picosecond-pumped OPCPA," Optica **5**, 434 (2018).

52. B. Zhao, J. Zhang, S. Chen, C. Liu, G. Golovin, S. Banerjee, K. Brown, J. Mills, C. Petersen, and D. Umstadter, "Wavefront-correction for nearly diffraction-limited focusing of dual-color laser beams to high intensities," Opt. Express **22**, 26947 (2014).
53. K. Zeil, S. D. Kraft, S. Bock, M. Bussmann, T. E. Cowan, T. Kluge, J. Metzkes, T. Richter, R. Sauerbrey, and U. Schramm, "The scaling of proton energies in ultrashort pulse laser plasma acceleration," New J. Phys. **12**, 045015 (2010).
54. P. F. Condamine, N. Jourdain, J. C. Hernandez, M. Taylor, H. Bohlin, A. Fajstavr, T. M. Jeong, D. Kumar, T. Laštovička, O. Renner, M. Nakatsutsumi, S. Alatabi, S. Aldawood, M. Amin, M. Andel, J. Andreasson, R. Angelova, P. Antici, M. Bakeman, and S. Weber, "High-repetition rate solid target delivery system for PW-class laser-matter interaction at ELI Beamlines," Rev. Sci. Instr. **92**, 063504 (2021).
55. S. Borneis, T. Laštovička, M. Sokol, T.-M. Jeong, F. Condamine, O. Renner, V. Tikhonchuk, H. Bohlin, A. Fajstavr, J.-C. Hernandez, N. Jourdain, D. Kumar, D. Modřanský, A. Pokorný, A. Wolf, S. Zhai, G. Korn, and S. Weber, "Design, installation and commissioning of the ELI-Beamlines high-power, high-repetition rate HAPLS laser beam transport system to P3," High Power Laser Sci. Eng. **9**, e30 (2021).
56. S. Kühn, M. Dumergue, S. Kahaly, S. Mondal, M. Füle, T. Csizmadia, B. Farkas, B. Major, Z. Várallyay, E. Cormier, M. Kalashnikov, F. Calegari, M. Devetta, F. Frassetto, E. Månsson, L. Poletto, S. Stagira, C. Vozzi, M. Nisoli, P. Rudawski, S. Maclot, F. Campi, H. Wikmark, C. L. Arnold, C. M. Heyl, P. Johnsson, A. L'Huillier, R. Lopez-Martens, S. Haessler, M. Bocoum, F. Boehle, A. Vernier, G. Iaquaniello, E. Skantzakis, N. Papadakis, C. Kalpouzos, P. Tzallas, F. Lépine, D. Charalambidis, K. Varjú, K. Osvay, and G. Sansone, "The ELI-ALPS facility: the next generation of attosecond sources," J. Phys. B: At. Mol. Opt. Phys. **50**, 132002 (2017).
57. D. A. Jaroszynski, B. Ersfeld, M. R. Islam, E. Brunetti, R. P. Shanks, P. A. Grant, M. P. Tooley, D. W. Grant, D. Reboredo Gil, P. Lepipas, G. McKendrick, S. Cipiccia, S. M. Wiggins, G. H. Welsh, G. Vieux, S. Chen, C. Aniculaesei, G. G. Manahan, M.-P. Anania, A. Noble, S. R. Yoffe, G. Raj, A. Subiel, X. Yang, Z. M. Sheng, B. Hidding, R. C. Issac, M.-H. Cho, and M. S. Hur, "Coherent radiation sources based on laser driven plasma waves," in *Proceedings of 40th International Conference on IRMMW-THz* (2015), paper H2E-1.

58. L. Roso, “Salamanca Pulsed Laser Center: the Spanish petawatt,” Proc. SPIE **8001**, 800113 (2011).
59. L. Roso, “High repetition rate Petawatt lasers,” EPJ Web Conf. **167**, 01001 (2018).
60. S. Formaux, S. Payeur, A. Alexandrov, C. Serbanescu, F. Martin, T. Ozaki, A. Kudryashov, and J. C. Kieffer, “Laser beam wavefront correction for ultra high intensities with the 200 TW laser system at the Advanced Laser Light Source,” Opt. Express **16**, 11987 (2008).
61. L. A. Gizzi, C. Benedetti, C. Alberto Cecchetti, G. Di Pirro, A. Gamucci, G. Gatti, A. Giulietti, D. Giulietti, P. Koester, L. Labate, T. Levato, N. Pathak, and F. Piastra, “Laser-Plasma Acceleration with FLAME and ILIL Ultraintense Lasers,” Appl. Sci. **3**, 559 (2013).
62. H. S. Peng, W. Y. Zhang, X. M. Zhang, Y. J. Tang, W. G. Zheng, Z. J. Zheng, X. F. Wei, Y. K. Ding, Y. Gou, S. P. Zhou, and W. B. Pei, “Progress in ICF programs at CAEP,” Lasers Part. Beams **23**, 205 (2005).
63. A. Moulet, S. Grabielle, C. Cornaggia, N. Forget, and T. Oksenhendler, “Single-shot, high-dynamic-range measurement of sub-15 fs pulses by self-referenced spectral interferometry,” Opt. Lett. **35**, 3856 (2010).
64. S. Lorenz, G. Grittani, K. Kondo, A. Kon, Y.-K. Liu, A. Sagisaka, K. Ogura, N. Nakanii, K. Huang, A. Bierwage, S. Namba, H. Ohiro, T. A. Pikuz, J. K. Koga, P. Chen, H. Kiriyama, M. Kando, T. Zh. Esirkepov, S. V. Bulanov, and A. S. Pirozhkov, “In-vacuum post-compression of optical probe pulse for relativistic plasma diagnostics,” Optica Open, 107298 (2013). https://doi.org/10.1364/opticaopen.23559879.v2.
65. F. Consoli, V. T. Tikhonchuk, M. Bardon, P. Bradford, D. C. Carroll, J. Cikhardt, M. Cipriani, R. J. Clarke, T. E. Cowan, C. N. Danson, R. De Angelis, M. De Marco, J.-L. Dubois, B. Etchessahar, A. L. Garcia, D. I. Hillier, A. Honsa, W. Jiang, V. Kmetik, J. Krása, Y. Li, F. Lubrano, P. McKenna, J. Metzkes-Ng, A. Poyé, I. Prencipe, P. Rączka, R. A. Smith, R. Vrana, N. C. Woolsey, E. Zemaityte, Y. Zhang, Z. Zhang, B. Zielbauer, and D. Neely, “Laser produced electromagnetic pulses: generation, detection and mitigation,” High Power Laser Sci. Eng. **8**, e22 (2020).
66. A. Sagisaka, A. S. Pirozhkov, H. Daido, A. Fukumi, Z. Li, K. Ogura, A. Yogo, Y. Oishi, T. Nayuki, T. Fujii, K. Nemoto, S. Orimo, M. Nishiuchi, Y. Hayashi, M. Mori, M. Kado,

S. Nakamura, A. Noda, I. W. Choi, J. H. Sung, D.-K. Ko, and J. Lee, "Development of a two-color interferometer for observing wide range electron density profiles with a femtosecond time resolution," Appl. Phys. B **84**, 415 (2006).

67. A. S. Pirozhkov, I. W. Choi, J. H. Sung, S. K. Lee, T. J. Yu, T. M. Jeong, I. J. Kim, N. Hafz, C. M. Kim, K. H. Pae, Y.-C. Noh, D.-K. Ko, J. Lee, A. P. L. Robinson, P. J. Foster, S. J. Hawkes, M. Streeter, C. Spindloe, P. McKenna, D. C. Carroll, C.-G. Wahlström, M. Zepf, D. Adams, B. Dromey, K. Markey, S. Kar, Y. T. Li, M. H. Xu, H. Nagatomo, M. Mori, A. Yogo, H. Kiriyama, K. Ogura, A. Sagisaka, S. Orimo, M. Nishiuchi, H. Sugiyama, T. Zh. Esirkepov, H. Okada, S. Kondo, S. Kanazawa, Y. Nakai, A. Akutsu, T. Motomura, M. Tanoue, T. Shimomura, M. Ikegami, I. Daito, M. Kando, T. Kameshima, P. Bolton, S. V. Bulanov, H. Daido, and D. Neely, "Diagnostic of laser contrast using target reflectivity," Appl. Phys. Lett. **94**, 241102 (2009).
68. M. J. V. Streeter, P. S. Foster, F. H. Cameron, M. Borghesi, C. Brenner, D. C. Carroll, E. Divall, N. P. Dover, B. Dromey, P. Gallegos, J. S. Green, S. Hawkes, C. J. Hooker, S. Kar, P. McKenna, S. R. Nagel, Z. Najmudin, C. A. J. Palmer, R. Prasad, K. E. Quinn, P. P. Rajeev, A. P. L. Robinson, L. Romagnani, J. Schreiber, C. Spindloe, S. Ter-Avetisyan, O. Tresca, M. Zepf, and D. Neely, "Relativistic plasma surfaces as an efficient second harmonic generator," New J. Phys. **13**, 023041 (2011).
69. S. Singh, C. D. Armstrong, N. Kang, L. Ren, H. Liu, N. Hua, D. R. Rusby, O. Klimo, R. Versaci, Y. Zhang, M. Sun, B. Zhu, A. Lei, X. Ouyang, L. Lancia, A. Laso Garcia, A. Wagner, T. Cowan, J. Zhu, T. Schlegel, S. Weber, P. McKenna, D. Neely, V. Tikhonchuk, and D. Kumar, "Bremsstrahlung emission and plasma characterization driven by moderately relativistic laser–plasma interactions," Plasma Phys. Control. Fusion **63**, 035004 (2021).
70. N. N. Kolachevsky, A. S. Pirozhkov, and E. N. Ragozin, "Broadband x-ray optical elements based on aperiodic multilayer structures," Quantum Electron. **30**, 428 (2000).
71. E. A. Vishnyakov, F. F. Kamenets, V. V. Kondratenko, M. S. Luginin, A. V. Panchenko, Yu. P. Pershin, A. S. Pirozhkov, and E. N. Ragozin, "Aperiodic multilayer structures in soft X-ray radiation optics," Quantum Electron. **42**, 143 (2012).
72. A. S. Pirozhkov and E. N. Ragozin, "Aperiodic multilayer structures in soft X-ray optics," Phys. Usp. **58**, 1095 (2015).

73. E. A. Vishnyakov, K. N. Mednikov, A. A. Pertsov, E. N. Ragozin, A. A. Reva, A. S. Ul'yanov, and S. V. Shestov, "Measurements of reflection spectra of soft X-ray multilayer mirrors using a broadband laser-plasma radiation source," Quantum Electron. **39**, 474 (2009).
74. E. N. Ragozin, K. N. Mednikov, A. A. Pertsov, A. S. Pirozhkov, A. A. Reva, S. V. Shestov, A. S. Ul'yanov, and E. A. Vishnyakov, "Spectroscopic characterization of novel multilayer mirrors intended for astronomical and laboratory applications," Proc. SPIE **7360**, 73600N (2009).
75. M. M. Barysheva, S. A. Garakhin, A. O. Kolesnikov, A. S. Pirozhkov, V. N. Polkovnikov, E. N. Ragozin, A. N. Shatokhin, R. M. Smertin, M. V. Svechnikov, and E. A. Vishnyakov, "Broadband normal-incidence mirrors for a range of 111–138 Å based on an a-periodic Mo/Be multilayer structure," Opt. Mater. Express **11**, 3038 (2021).
76. E. A. Vishnyakov, A. O. Kolesnikov, A. A. Kuzin, D. V. Negrov, E. N. Ragozin, P. V. Sasorov, and A. N. Shatokhin, "Imaging diffraction VLS spectrometer for a wavelength range $\lambda > 120$ Å," Quantum Electron. **47**, 54 (2017).
77. A. N. Shatokhin, A. O. Kolesnikov, P. V. Sasorov, E. A. Vishnyakov, and E. N. Ragozin, "High-resolution stigmatic spectrograph for a wavelength range of 12.5–30 nm," Opt. Express **26**, 19009 (2018).
78. M. Kando, A. S. Pirozhkov, K. Kawase, T. Zh. Esirkepov, Y. Fukuda, H. Kiriyama, H. Okada, I. Daito, T. Kameshima, Y. Hayashi, H. Kotaki, M. Mori, J. K. Koga, H. Daido, A. Ya. Faenov, T. Pikuz, J. Ma, L.-M. Chen, E. N. Ragozin, T. Kawachi, Y. Kato, T. Tajima, and S. V. Bulanov, "Enhancement of Photon Number Reflected by the Relativistic Flying Mirror," Phys. Rev. Lett. **103**, 235003 (2009).
79. B. A. Volodin, S. A. Gusev, M. N. Drozdov, S. Yu. Zuev, E. B. Klyuenkov, A. Ya. Lopatin, V. I. Luchin, A. E. Pestov, N. N. Salashchenko, N. N. Tsybin, and N. I. Chkhalo, "Multilayer thin-film filters of extreme ultraviolet and soft X-ray spectral regions," Bull. Russ. Acad. Sci. Phys. **74**, 44 (2010).
80. E. A. Vishnyakov, A. S. Kirichenko, A. A. Reva, A. A. Rizvanov, Ju. A. Plastinin, and S. V. Kuzin, "Spectral calibration of CCDs and multilayer filters intended for future space applications," Proc. SPIE **9905**, Space Telescopes and Instrumentation 2016: Ultraviolet to gamma ray, 99053G (2016).

81. E. A. Vishnyakov, A. V. Shcherbakov, A. A. Pertsov, V. N. Polkovnikov, A. E. Pestov, D. E. Pariev, and N. I. Chkhalo, "High-aperture monochromator-reflectometer and its usefulness for CCD calibration," Proc. SPIE **10235**, EUV and X-ray Optics: Synergy between Laboratory and Space V, 102350W (2017).
82. C. D. Armstrong, "Bremsstrahlung radiation and fast electron transport in laser-plasma interactions," Ph.D. Thesis (University of Strathclyde, 2019).
83. D. R. Rusby, C. D. Armstrong, C. M. Brenner, R. J. Clarke, P. McKenna, and D. Neely, "Novel scintillator-based x-ray spectrometer for use on high repetition laser plasma interaction experiments," Rev. Sci. Instrum. **89**, 073502 (2018).
84. C. D. Armstrong, D. Neely, D. Kumar, P. McKenna, R. J. Gray, and A. S. Pirozhkov. "Deconvolution of multi-Boltzmann x-ray distribution from linear absorption spectrometer via analytical parameter reduction," Rev. Sci. Instrum. **92**, 113102 (2021).
85. A. Ya. Faenov, S. A. Pikuz, A. I. Erko, B. A. Bryunetkin, V. M. Dyakin, G. V. Ivanenkov, A. R. Mingaleev, T. A. Pikuz, V. M. Romanova, and T. A. Shelkovenko, "High-performance X-ray spectroscopic devices for plasma microsources investigations," Phys. Scr. **50**, 333 (1994).
86. J. P. Geindre, P. Audebert, A. Rousse, J. C. Gauthier, A. Ya. Faenov, T. A. Pikuz, S. A. Pikuz, and T. A. Shelkovenko, "FSSR mica spherical crystal spectrometer with CCD detector for high-resolution X-ray spectroscopy of femtosecond laser produced plasma," Phys. Scr. **53**, 645 (1996).
87. G. Hölzer, O. Wehrhan, J. Heinisch, E. Förster, T. A. Pikuz, A. Ya. Faenov, S. A. Pikuz, V. M. Romanova, and T. A. Shelkovenko, "Flat and Spherically Bent Muscovite (Mica) Crystals for X-ray Spectroscopy," Phys. Scr. **57**, 301 (1998).
88. D. Neely, D. Chambers, C. Danson, P. Norreys, S. Preston, F. Quinn, M. Roper, J. Wark, and M. Zepf, "A multi-channel soft X-ray flat-field spectrometer," AIP Conf. Proc. **426**, 479 (1998).
89. E. A. Vishnyakov, A. O. Kolesnikov, A. S. Pirozhkov, E. N. Ragozin, and A. N. Shatokhin, "Aperiodic reflective diffraction gratings for soft X-ray radiation and their application," Quantum Electron. **48**, 916 (2018).

90. E. N. Ragozin, E. A. Vishnyakov, A. O. Kolesnikov, A. S. Pirozhkov, and A. N. Shatokhin, “Soft X-ray spectrometers based on aperiodic reflection gratings and their application,” Phys.-Usp. **64**, 495 (2021).
91. U. Teubner and P. Gibbon, “High-order harmonics from laser-irradiated plasma surfaces,” Rev. Mod. Phys. **81**, 445 (2009).
92. C. Thaury and F. Quéré, “High-order harmonic and attosecond pulse generation on plasma mirrors: basic mechanisms,” J. Phys. B: At. Mol. Opt. Phys. **43**, 213001 (2010).
93. I. J. Kim, K. H. Pae, C. M. Kim, H. T. Kim, H. Yun, S. J. Yun, J. H. Sung, S. K. Lee, J. W. Yoon, T. J. Yu, T. M. Jeong, C. H. Nam, and J. Lee, "Relativistic frequency upshift to the extreme ultraviolet regime using self-induced oscillatory flying mirrors," Nat. Commun. **3**, 1231 (2012).
94. S. Kahaly, S. Monchocé, H. Vincenti, T. Dzelzainis, B. Dromey, M. Zepf, Ph. Martin, and F. Quéré, "Direct Observation of Density-Gradient Effects in Harmonic Generation from Plasma Mirrors," Phys. Rev. Lett. **110**, 175001 (2013).
95. S. V. Bulanov, N. M. Naumova, and F. Pegoraro, "Interaction of an ultrashort, relativistically strong laser pulse with an overdense plasma," Phys. Plasmas **1**, 745 (1994).
96. R. Lichters, J. Meyer-ter-Vehn, and A. Pukhov, “Short-pulse laser harmonics from oscillating plasma surfaces driven at relativistic intensity,” Phys. Plasmas **3**, 3425 (1996).
97. S. W. Bahk, P. Rousseau, T. A. Planchon, V. Chvykov, G. Kalintchenko, A. Maksimchuk, G. A. Mourou, and V. Yanovsky, “Generation and characterization of the highest laser intensities (10^{22} W/cm^2),” Opt. Lett. **29**, 2837 (2004).
98. G. Tiwari, E. Gaul, M. Martinez, G. Dyer, J. Gordon, M. Spinks, T. Toncian, B. Bowers, X. Jiao, R. Kupfer, L. Lisi, E. McCary, R. Roycroft, A. Yandow, G. D. Glenn, M. Donovan, T. Ditmire, and B. M. Hegelich, “Beam distortion effects upon focusing an ultrashort petawatt laser pulse to greater than 10^{22} W/cm^2,” Opt. Lett. **44**, 2764 (2019).

E.A. Vishnyakov et al. **"Metrology for sub-Rayleigh-length target positioning in ~10^{22} W/cm^2 laser-plasma experiments"**

Figures and tables

Fig. 1.

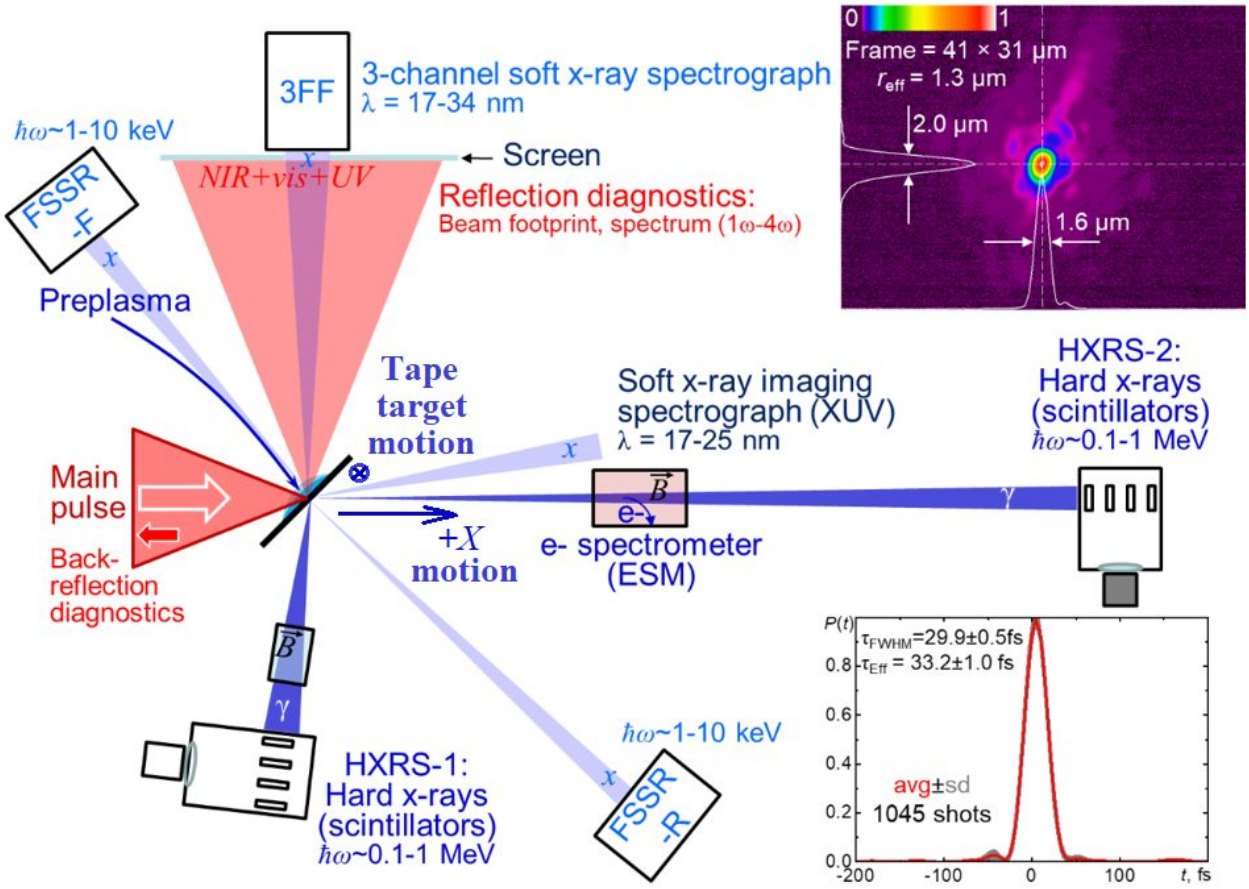

E.A. Vishnyakov et al. **"Metrology for sub-Rayleigh-length target positioning in ~10^{22} W/cm^2 laser-plasma experiments"**

Figures and tables

Fig. 2.

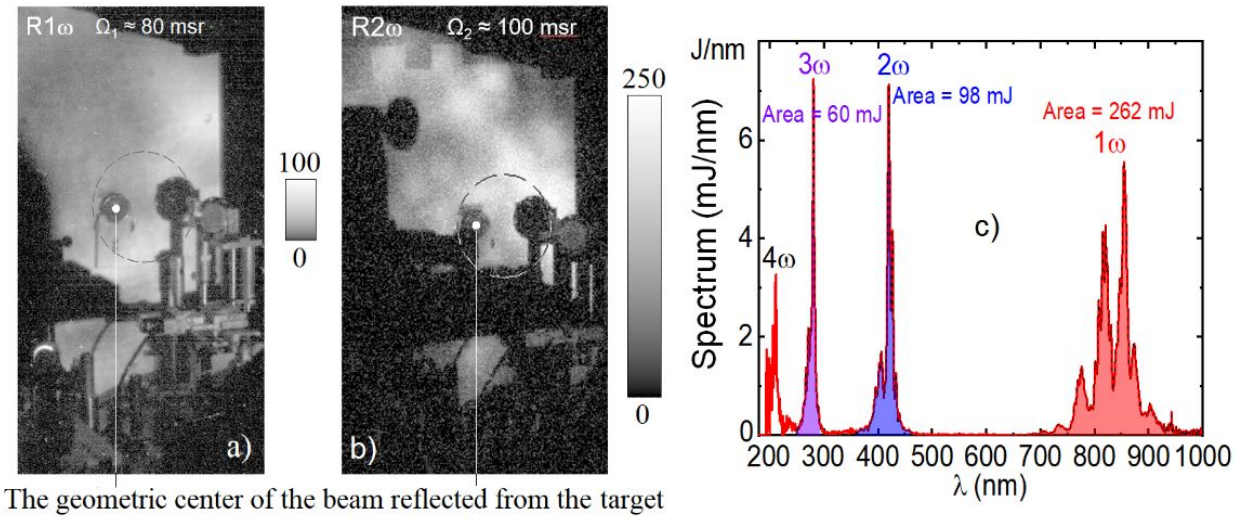

Figures and tables

Fig. 3.

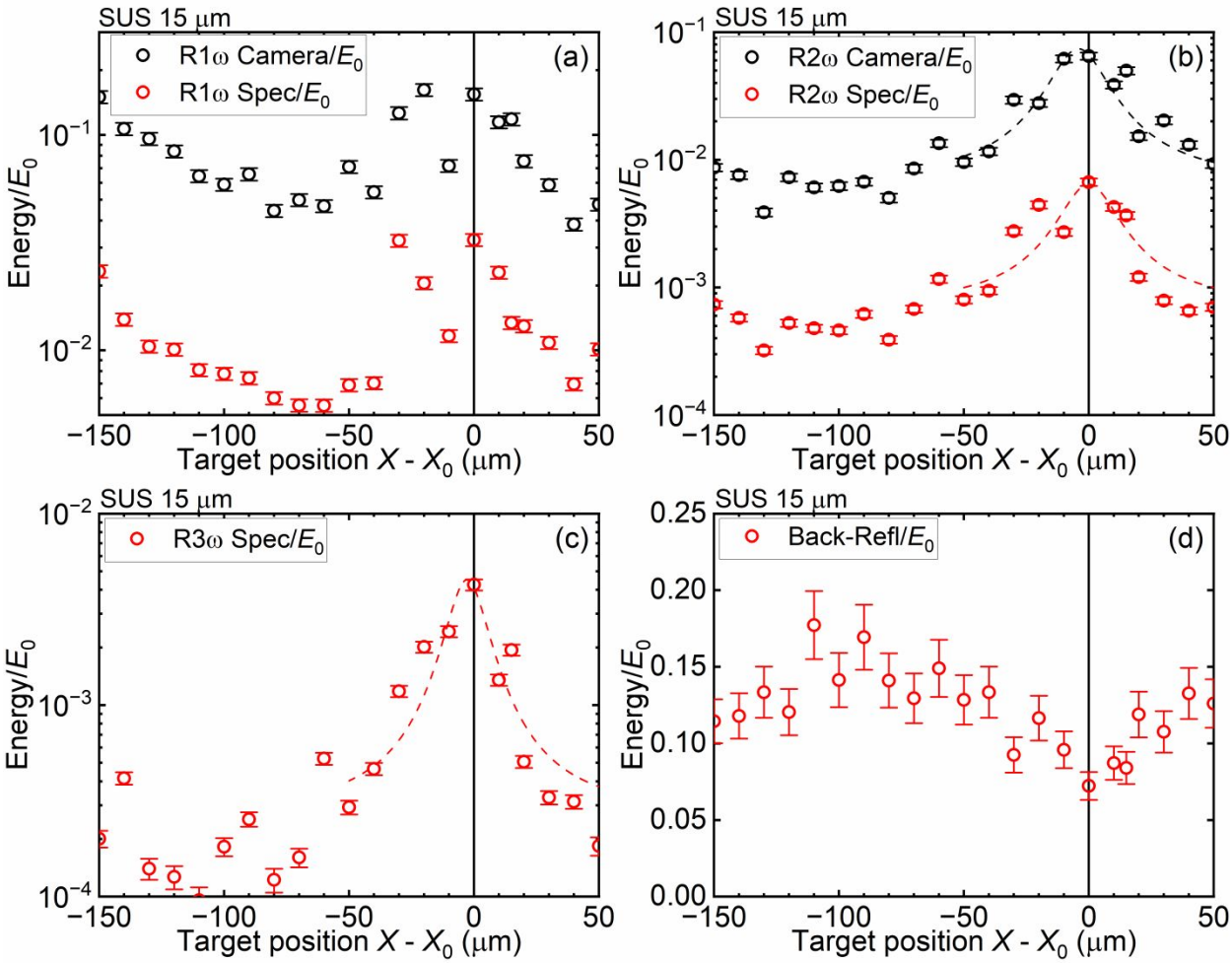

E.A. Vishnyakov et al. **"Metrology for sub-Rayleigh-length target positioning in ~10^{22} W/cm^2 laser-plasma experiments"**

Figures and tables

Fig. 4.

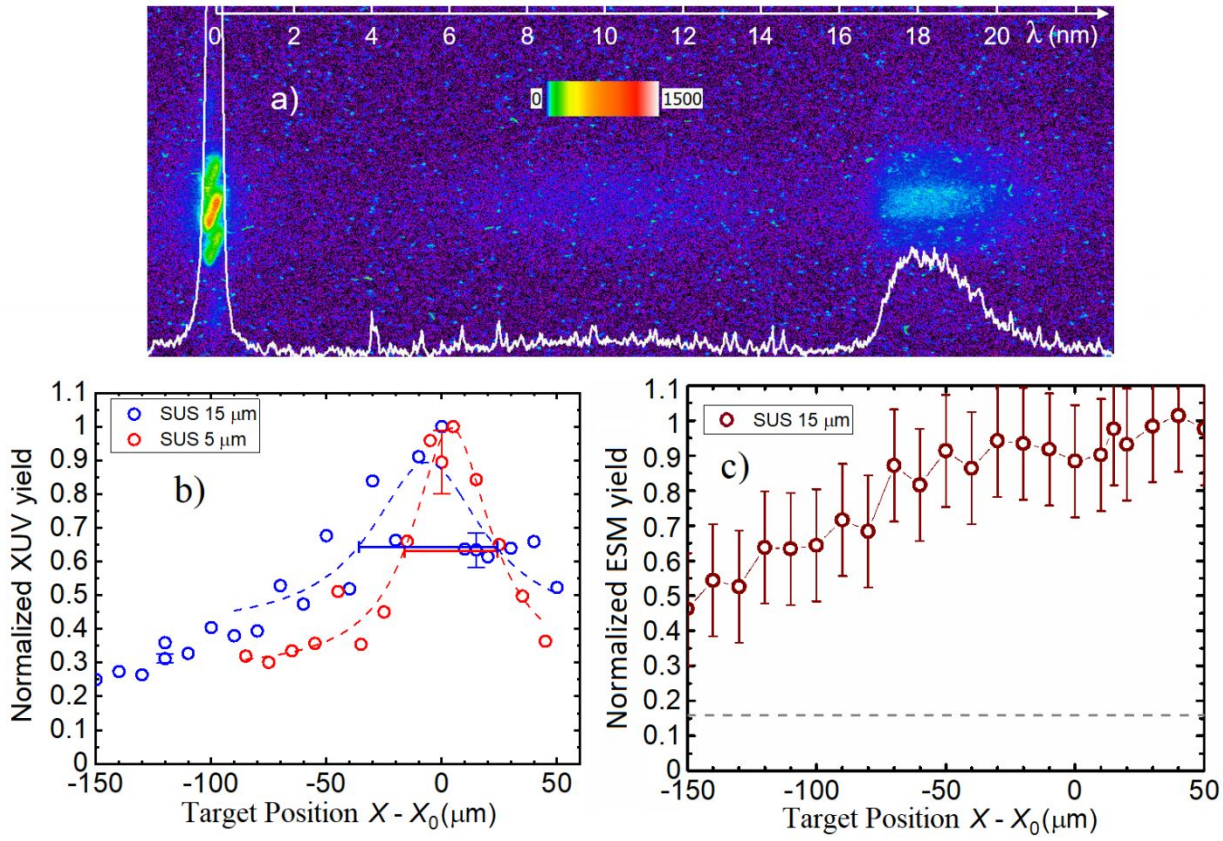

E.A. Vishnyakov et al. **"Metrology for sub-Rayleigh-length target positioning in ~10^{22} W/cm^2 laser-plasma experiments"**

Figures and tables

Fig. 5.

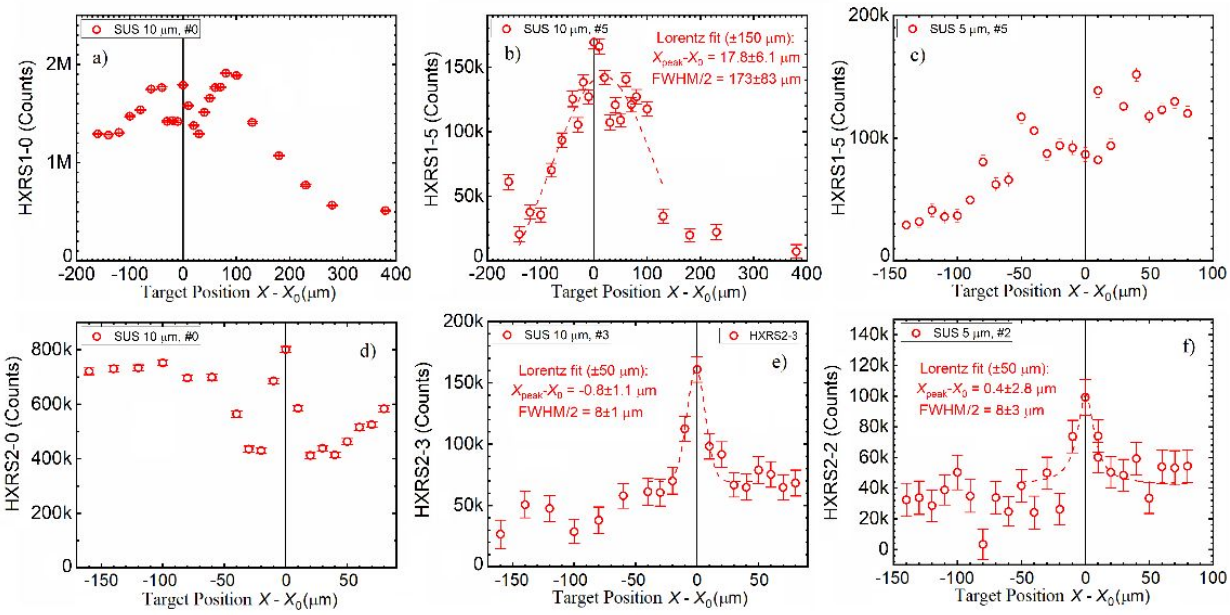

E.A. Vishnyakov et al. **"Metrology for sub-Rayleigh-length target positioning in ~10^{22} W/cm^2 laser-plasma experiments"**

Figures and tables

Fig. 6.

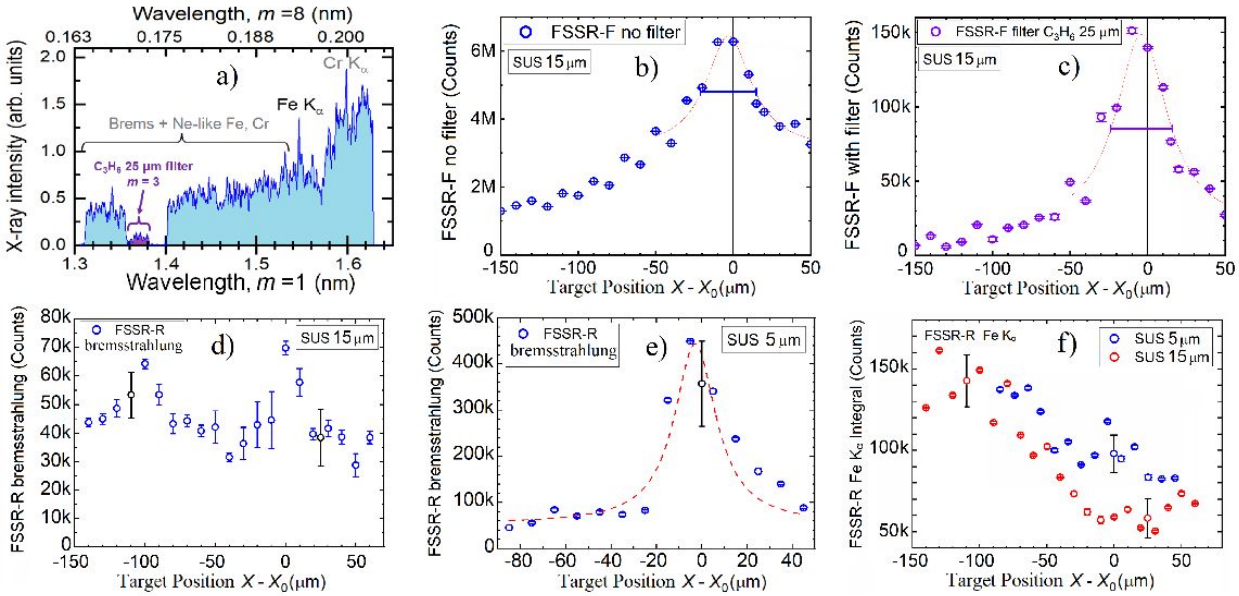

E.A. Vishnyakov et al. **"Metrology for sub-Rayleigh-length target positioning in ~10^{22} W/cm^2 laser-plasma experiments"**

Figures and tables

Fig. 7.

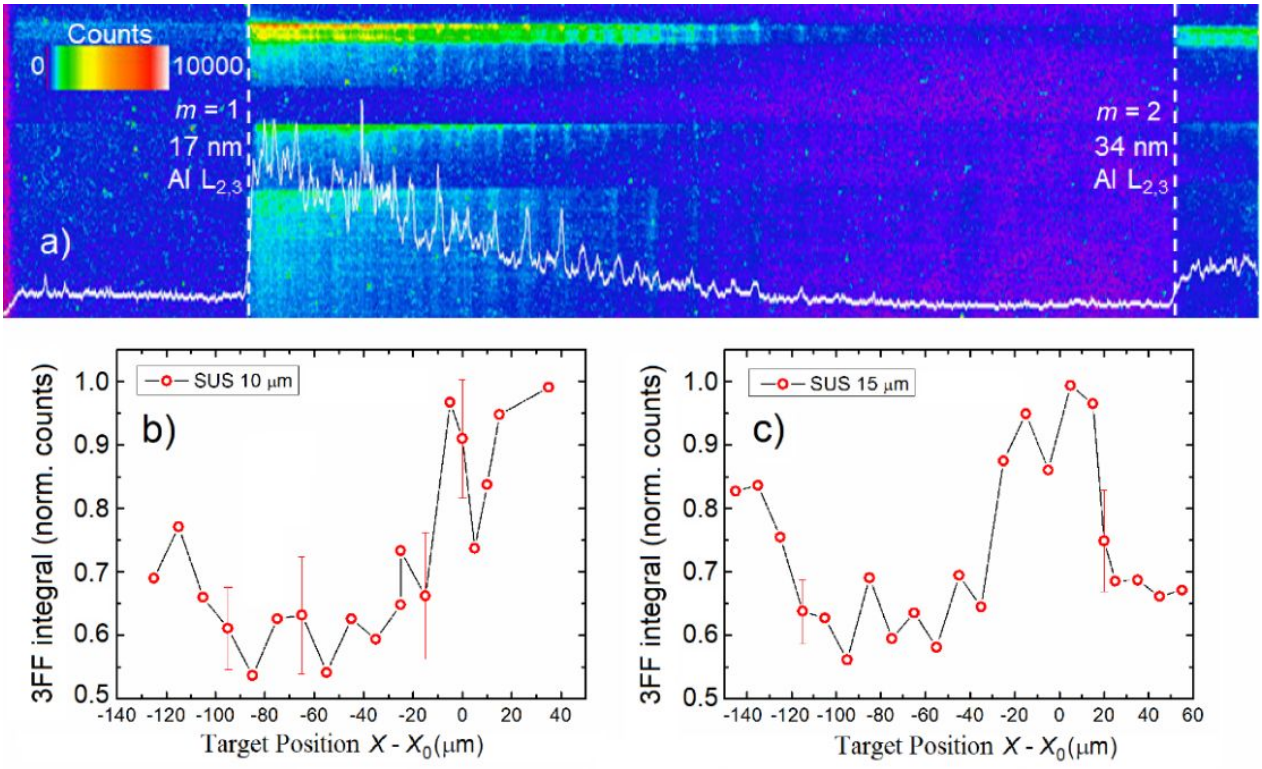

E.A. Vishnyakov et al. **"Metrology for sub-Rayleigh-length target positioning in ~10^{22} W/cm^2 laser-plasma experiments"**

Figures and tables

Table 1.

Name of the instrument	Peak FWHM, µm	Peak shift, µm	Estimated* accuracy, µm	Comment
Reflection 'specular direction' camera, 1ω	~60	~20	~30	Multi-peak
Reflection 'specular direction' camera, 2ω	24 ± 6	<5	~12	
Reflection 'specular direction' spectrometer, 1ω	~70	~30	~30	Multi-peak
Reflection 'specular direction' spectrometer, 2ω	24 ± 10	<5	~12	
Reflection 'specular direction' spectrometer, 3ω	18 ± 6	<4	~5	
Back-reflection camera	Not applicable			No peak
Rear-Side XUV – thin targets	40 ± 6	<5	~20	
Rear-Side XUV – thick targets	60 ± 26	<10	~30	Weak signal
Rear-Side ESM	~120	~40	~60	Plateau-like
Rear-Side HXRS-1 (off-axis) – thin targets	~120	~50	~60	No clear peak
Rear-Side HXRS-1 (off-axis)	~200	~20	~100	Broad

– thick targets				peak
Rear-Side HXRS-2 (on-axis) – thin targets	16 ± 6	<4	~5	Weak signal
Rear-Side HXRS-2 (on-axis) – thick targets	16 ± 2	<2.5	~5	
Front-Side FSSR-F	40 ± 10	<5	~20	
Rear-Side FSSR-R – bremsstrahlung integral	24 ± 8	<5	~12	Double-peak
Rear-Side FSSR-R – Fe K_α integral	Not applicable			Multi-peak
'Specular reflection' 3FF spectrometer – integral	~50	~10	~25	Multi-peak
'Specular reflection' 3FF spectrometer – HOH	~50	~10	~25	
'Specular reflection' 3FF spectrometer – central dip	~10	~5	~5	Contrast-dependent

*Estimated accuracy was a half-step size for the clean peaks, and a half-width at half-maximum (HWHM) for instruments with notable data fluctuations.

Figure and table captions

Fig. 1. Experimental scheme (not to scale). The J-KAREN-P laser pulses (Ø 280 mm, 33 fs, 10 J, λ_0 ~ 820 nm, p-polarized) were focused into an r_{eff} ~ 1.3 μm focal spot on a 5 – 20 μm stainless-steel tape target[26] mounted at a 45º incident angle. The observation direction of the back-reflection diagnostics at 1ω is shown by the red arrow. Several reflection diagnostics (1ω and 2ω imagers, 1ω – 4ω fiber spectrometer) measured the reflected beam footprint on a screen mounted perpendicular to the 'specular reflection' direction; a three-channel flat-field XUV spectrograph (3FF) was mounted behind a hole in the screen. The first hard X-ray spectrometer HXRS-1 was mounted 98º off the main laser pulse direction. The second hard X-ray spectrometer HXRS-2 and an electron spectrometer (ESM) were along the direction of the main laser pulse, while the imaging XUV spectrograph was 12º off this direction. $\vec{B}$ symbols stand for dipole magnets removing electrons from HXRS-1,2 and dispersing electrons in the electron spectrometer ESM. Two soft X-ray spectrometers with spatial resolution (FSSR) were mounted on the target front (-F) and rear (-R) sides, 7.85° and 10.3° from the target normal in-plane, and 17.85° and 23.6° out-of-plane angles, respectively. The insets show spatial and temporal J-KAREN-P laser pulse profiles. A tape target of 20 mm width was mounted on a double-rotating-reel setup, which could be translated linearly along the laser axis with a 0.1-μm step size (the '–' sign denotes direction towards the OAP).

Fig. 2. The fields of view of the 1ω (a) and 2ω (b) cameras imaging a PTFE screen mounted perpendicular to the 'specular reflection' direction. The geometric center of the reflected beam is marked with the white circles. The dashed ellipses denote the spectrometer observation area. (c) Typical absolutely-calibrated reflected spectrum. The energy values calculated within the $(n \pm 0.25)\cdot\omega_0$ spectral bandwidths (colored) are given for harmonic orders n = 1,2,3.

Fig. 3. Normalized energy from the four reflection beam diagnostics versus the target position X ('–' denotes the direction towards the OAP, and X_0 corresponds to the best focus position). All values are normalized by the on-target pulse energy E_0. The plots in (a) and (b) are for the 1ω and 2ω diagnostics, respectively, where the upper data (black) are from the imagers, while the lower data (red) are integrated from the 1ω – 4ω spectrometer within $(1 \pm 0.25)\cdot\omega_0$ and $(2 \pm 0.25)\cdot\omega_0$, correspondingly. (c) 3ω data integrated within the $(3 \pm 0.25)\cdot\omega_0$ band from the 1ω – 4ω spectrometer. (d) shows the normalized back-reflected energy.

Fig. 4. a) Typical spatially-resolved XUV spectrum; λ = 0 denotes the 0th diffraction order. b) Dependence of the integrated 0th order on the target position ('–' is towards the OAP) for 5-μm and 15-μm-thick targets, and their Lorentzian fits. c) Dependence of the integrated ESM yield on the target position for a 15-μm-thick target. The dashed line shows the ESM noise level.

Fig. 5. HXRS scintillator plate signals vs. target position X ('−'is towards the OAP, X_0 is the best focus). (a-c) HXRS-1 (off-axis), (d-f) HXRS-2 (on-axis). a) HXRS-1 plate #0, 10-μm-thick SUS. b) HXRS-1 plate #5, 10-μm-thick SUS. c) HXRS-1 plate #5, 5-μm-thick SUS. Here, the large error bar corresponds to statistical (i. e. shot-to-shot variation) errors, while the smaller error bars in all frames are due to the CMOS camera noise. d) HXRS-2 plate #0, 10-μm-thick SUS film. e) HXRS-2 plate #3, 10-μm-thick SUS. f) HXRS-2 plate #2, 5-μm-thick SUS. Lorentzian fits are shown, where applicable. Scintillator plate #0 was the closest to the interaction point.

Fig. 6. a) A typical FSSR-F spectrum recorded in the vicinity of the best in-focus target position. The spectrum covers wavelengths from 0.165 nm to 1.63 nm in different diffraction orders from $m = 1$ to $m = 8$. Strong characteristic lines Fe K_α ($\lambda = 0.194$ nm) and Cr K_α ($\lambda = 0.229$ nm) were observed in $m = 8$ and $m = 7$ diffraction orders, respectively. The continuous signal corresponds to bremsstrahlung. A narrow strip of a 25-μm C_3H_6 filter allows observing a narrow portion of the spectrum, suppressing emission from lower diffraction orders ($m = 1$, $m = 2$). (b, c) FSSR-F data for 15-μm SUS targets, integrated within an area without (b) and with (c) the 25-μm-thick C_3H_6 filter. (d, e) FSSR-R integrated bremsstrahlung signal for 15-μm (d) and 5-μm (e) SUS targets. f) FSSR-R Fe K_α integrated signals for 15-μm and 5-μm SUS targets. The black error bars correspond to statistical shot-to-shot signal variations, while the smaller colored error bars are due to CCD camera noise. Lorentzian fits are shown, where applicable.

Fig. 7. a) 3FF spectrum with harmonics. The upper and lower parts correspond to the shallow- and high-deviation-angle mirrors, respectively. (b, c): integrated 3FF signal vs. target position for 10-μm and 15-μm SUS targets, respectively. The error bars correspond to shot-to-shot signal variations. Dashed lines show the Al filter cutoff (λ = 17 nm) in the 1st and 2nd diffraction orders.

Table captions

Table 1. Accuracy of the instruments for the best *in-focus* target positioning.